12-2003

Itera- tive Reconstruction Framework for High-Resolution X-ray CT Data

Thomas Matthew Benson
University of Tennessee - Knoxville

To the Graduate Council:

I am submitting herewith a thesis written by Thomas Matthew Benson entitled "Itera- tive Reconstruction Framework for High-Resolution X-ray CT Data." I have examined the final electronic copy of this thesis for form and content and recommend that it be accepted in partial fulfillment of the requirements for the degree of Master of Science, with a major in Computer Science.

Jens Gregor, Major Professor

We have read this thesis and recommend its acceptance:

Jian Huang, Michael Thomason

Accepted for the Council:
Carolyn R. Hodges

Vice Provost and Dean of the Graduate School

(Original signatures are on file with official student records.)

To the Graduate Council:

I am submitting herewith a thesis written by Thomas Matthew Benson entitled "Iterative Reconstruction Framework for High-Resolution X-ray CT Data." I have examined the final electronic copy of this thesis for form and content and recommend that it be accepted in partial fulfillment of the requirements for the degree of Master of Science, with a major in Computer Science.

Jens Gregor

Dr. Jens Gregor, Major Professor

We have read this thesis
and recommend its acceptance:

Jian Huang

Michael Thomason

Accepted for the Council:

Anne Mayhew

Vice Provost and Dean of Graduate Studies

(Original signatures are on file with official student records.)

Iterative Reconstruction Framework for High-Resolution X-ray CT Data

A Thesis

Presented for the

Master of Science

Degree

The University of Tennessee, Knoxville

Thomas M. Benson

December, 2003

Acknowledgments

I would like to thank Dr. Jens Gregor for devoting a great deal of time to advising me during this work. His assistance has been crucial during the course of this thesis and is much appreciated. I would also like to thank my family for their continued support during my prolonged affiliation with the educational system.

This work was supported by the National Institutes of Health under grant number 1 R01 EB00789-01A2. The computer equipment was acquired as part of SInRG, a University of Tennessee grid infrastructure grant supported by the National Science Foundation under grant number EIA-9972889.

Abstract

Small animal medical imaging has become an important tool for researchers as it allows noninvasively screening animal models for pathologies as well as monitoring disease progression and therapy response. Currently, clinical CT scanners typically use a Filtered Backprojection (FBP) based method for image reconstruction. This algorithm is fast and generally produces acceptable results, but has several drawbacks. Firstly, it is based upon line integrals, which do not accurately describe the process of X-ray attenuation. Secondly, noise in the projection data is not properly modeled with FBP. On the other hand, iterative algorithms allow the integration of more complicated system models as well as robust scatter and noise correction techniques. Unfortunately, the iterative algorithms also have much greater computational demands than their FBP counterparts. In this thesis, we develop a framework to support iterative reconstructions of high-resolution X-ray CT data. This includes exploring various system models and algorithms as well as developing techniques to manage the significant computational and system storage requirements of the iterative algorithms. Issues related to the development of this framework as well as preliminary results are presented.

Contents

List of Tables

List of Figures

Chapter 1

Introduction

Small animal medical imaging has become an important tool for researchers as it allows noninvasively screening animal models for pathologies as well as monitoring disease progression and therapy response. In support of the Mammalian Genetics Research Facility at Oak Ridge National Laboratory, an X-ray micro-CT scanner, the MicroCAT™ (ImTek, Inc., TN), has been developed for the imaging of laboratory mice [4], [10]. This scanner has since been transferred to industry for commercialization.

The MicroCAT scanner acquires projection data of an object using a cone beam geometry, which will be illustrated shortly. The MicroCAT acquires projections on a CCD/phosphor screen detector. The CCD array is bonded to the phosphor screen, which is sensitive to X-ray energies, using a 2:1 fiber optic taper. The X-ray source and detector move in tandem in a circular orbit around the object. The geometry for the MicroCAT is shown in figure 1.1.

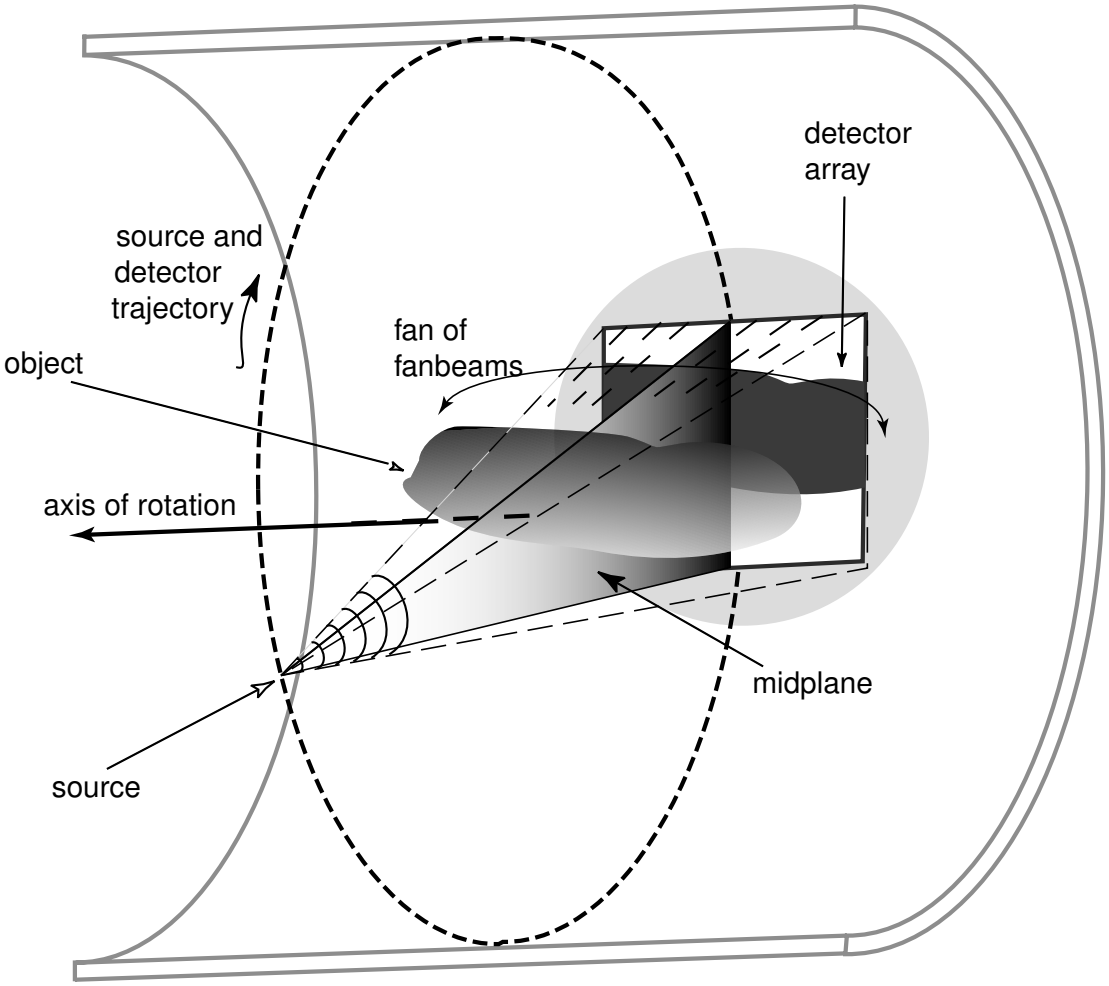

Figure 1.1. MicroCAT geometry (courtesy of J. Cates)

Note that the X-rays transmitted from the source form a cone as they diverge from the source toward the detector. Hence, this geometry is referred to as a cone beam geometry. A scan of an object is completed by recording the projection data, which is collected at the detector, for some number of view angles. Once this data is collected, the object must be reconstructed using the projection data and knowledge of the scanner.

There are three major classes of algorithms available for X-ray CT image reconstruction: exact, approximate, and iterative algorithms [14]. The exact algorithms require data sufficiency conditions that are very difficult to satisfy in practice, especially for a cone beam geometry. Thus, exact algorithms are rarely used to reconstruct real world data.

The class of approximate algorithms includes the most frequently used algorithm for reconstructing X-ray CT data: the Filtered Backprojection (FBP) based algorithm introduced by Feldkamp et al [3]. This FBP algorithm is popular because it is fast and generally produces good results. However, FBP has a few drawbacks. In particular, the projection data is assumed to represent line integrals through an object, which does not accurately describe the process of X-ray attenuation. Furthermore, it is difficult to account for the noise and scatter which are present in real projection data when using the FBP algorithm.

On the other hand, the iterative algorithms facilitate more complicated system models than line integrals. It is also possible to account for scatter and other additive noise factors using the iterative algorithms, although this requires modeling the processes

involved. The major drawback to the iterative algorithms is the massively increased storage and computational requirements. Due to these increased costs, iterative algorithms are rarely used for three dimensional X-ray CT reconstructions. However, iterative algorithms are heavily used for Positron Emission Tomography (PET) and Single Photon Emission Computed Tomography (SPECT) due to the lower computational requirements and increased noise and scatter levels.

As computer technology advances, three dimensional iterative CT reconstructions are becoming more feasible. The goal of this thesis is to develop a framework to support high-resolution iterative reconstructions of X-ray CT data. This framework needs to provide mechanisms to compute and store a very large system matrix and to perform iterative solution techniques using this system matrix. Furthermore, the framework should support easily replacing the system model used to compute the system matrix and the iterative algorithm used to approximate a solution. Once developed, we can utilize this framework to perform feasibility studies and comparative analysis on various system models and iterative algorithms used for iterative X-ray CT reconstructions.

The decision to store the system matrix is rather unique. In general, due to the massive space requirements involved in storing the system matrix, the matrix values are recomputed as needed. However, since the entire matrix is needed for each iteration, these values must be recomputed at least once per iteration. For most iterative algorithms, the matrix values are actually needed twice per iteration. One of the design goals of our iterative reconstruction framework is to avoid recomputing the system ma-

trix to increase performance. Note that there is also a body of literature exploring the use of different system models based upon the operation being performed. These are referred to as unmatched projectors [17] and are used to reduce the computation time involved in generating the system matrix. However, since we store the system matrix, we do not explore the use of unmatched projectors.

The first step of this thesis is to derive the reconstruction problem in terms of a linear system and define each of the components of that linear system. This involves describing the nature of the available data and some potential system models. The system models include line intersection based models and a trilinear interpolation based model. A fast algorithm for finding the intersections for the line intersection based models was proposed by Siddon [13] and improved by Jacobs et al [5]. We address these issues in chapter 2.

After stating the reconstruction problem in terms of a linear system, we must evaluate potential solutions of the linear system. These solutions take the form of iterative algorithms and are introduced in chapter 3. The algorithms used in this thesis include the Simultaneous Algebraic Reconstruction Technique (SART) proposed by Andersen and Kak [6], the Expectation Maximization (EM) algorithm proposed independently by Shepp and Vardi [12] and Lange and Carson [7], and a Weighted Least Squares technique proposed by Fessler [2].

Due to the potentially massive size of the system matrix, we must address matrix storage issues, which is the goal of chapter 4. Techniques used to manage the system ma-

trix include sparse matrix storage, the exploitation of symmetries, and load distribution via the Message Passing Interface (MPI).

We present results of this work in chapter 5. These results include a preliminary system model analysis as well as several iterative reconstructions. We also address the system matrix storage and timing requirements for several reconstructions. Finally, chapter 6 contains the conclusions as well as possible directions for future work.

Chapter 2

Image Reconstruction as a Linear System

The first step in reconstructing images from a data set is to represent the reconstruction problem in mathematical terms so that a solution can be deduced or approximated. For many of the iterative reconstruction algorithms, including all algorithms considered in this thesis, the basic mathematical model takes the form of a linear system. We formulate the general structure of this linear system in the following sections.

2.1 Mathematical Foundations

The goal of X-ray computed tomography is to reconstruct some object based only on projections of that object. Essentially, projection data records the effects of a given object on an X-ray beam along a known path. Based on this data, we can reconstruct

an approximate attenuation map of the scanned object. For the purposes of this thesis, an attenuation map is a collection of values that describes, in relative terms, the influence of a spatial location on the attenuation of an X-ray beam. When discretized into a three dimensional voxel space, the value of each voxel represents the average effect of that voxel on the attenuation of the X-ray. We can then directly visualize the object by interpreting the coefficients of the attenuation map as gray scale intensity values.

2.1.1 Projections

Before we state the reconstruction problem in mathematical terms, it is important to formally introduce the concepts of projections and attenuation. Consider the system depicted in figure 2.1. This system is using a parallel beam geometry where the source is t units from the origin of a coordinate system which is tilted θ degrees from the original coordinate system. The source emits an X-ray beam through the object $f(x, y)$ along the line $x\cos\theta + y\sin\theta = t$. Denote this line as (θ, t) and the line integral of (θ, t) as $P_\theta(t)$. Then,

$$P_\theta(t) = \int_{(\theta,t)} f(x, y)\, ds. \tag{2.1}$$

The function $P_\theta(t)$ is known as the Radon transform of the function $f(x, y)$. We can rewrite the Radon transform using the delta function as

$$P_\theta(t) = \int_{-\infty}^{\infty}\int_{-\infty}^{\infty} f(x, y)\, \delta(x\cos\theta + y\sin\theta - t)\, dx\, dy. \tag{2.2}$$

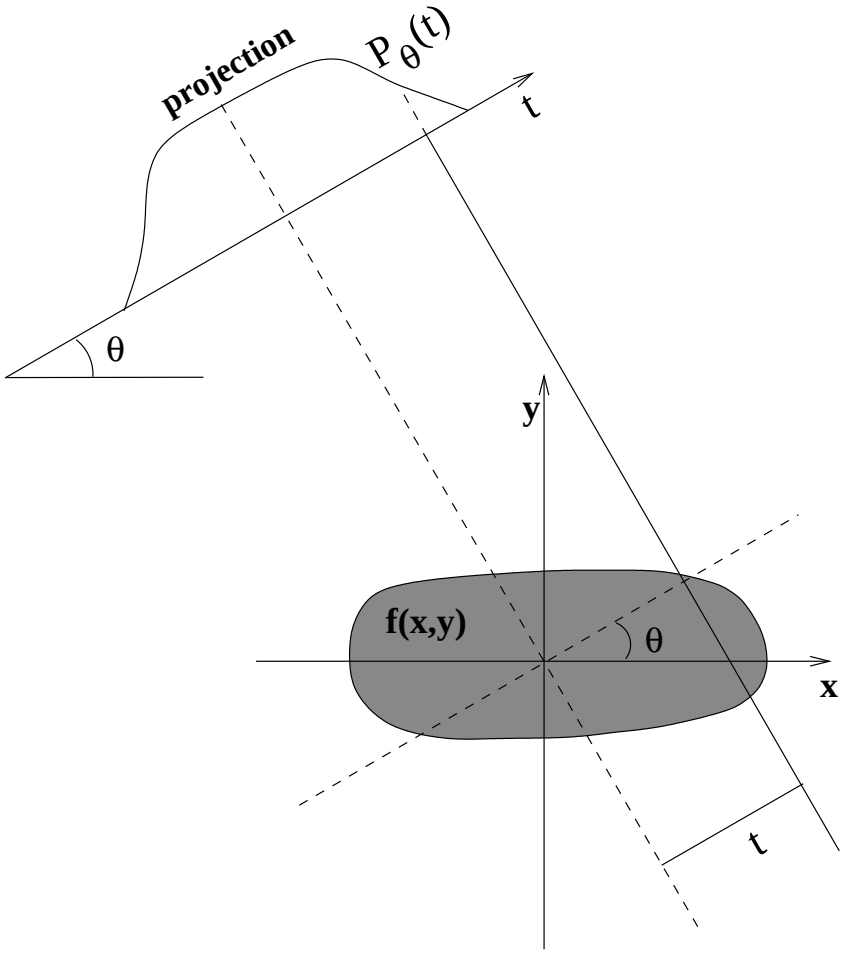

Figure 2.1. Radon transform geometry

A projection consists of a collection of line integrals with varying t values for a particular θ value. In the case of a fan beam geometry, the t values correspond to some angular offset from the line connecting the X-ray source to the axis of rotation. A cone beam geometry includes an additional angular offset to account for variation in the z direction.

A set of projections is often referred to as a sinogram because a point (x, y) in the object space maps to a sinusoid in the projection space. For example, consider some point (x, y) in the object space and let (r, ϕ) denote its polar coordinates. Then, in the projection space, (r, ϕ) maps to the sinusoid $(\theta, r\,cos(\phi - \theta))$. Figure 2.2 is a fanbeam sinogram of a mouse scanned in the MicroCAT scanner. The sinusoidal characteristics of the data are evident.

2.1.2 X-Ray Attenuation

Since a detector records photon counts rather than line integrals associated with some projection ray, we must interpret the data to yield approximations to the line integrals given in equation (2.2). This involves modeling the process of attenuation that an X-ray beam undergoes while passing through an object.

There are two primary causes for the attenuation of an X-ray: Compton scatter and the photoelectric effect. The photoelectric effect involves the absorption of photon energy by an inner electron of an atom such that the electron is freed from the atom. Compton scatter involves the interaction of a photon with a free or loosely bound electron, which results in the deflection of the photon and a transference of energy from

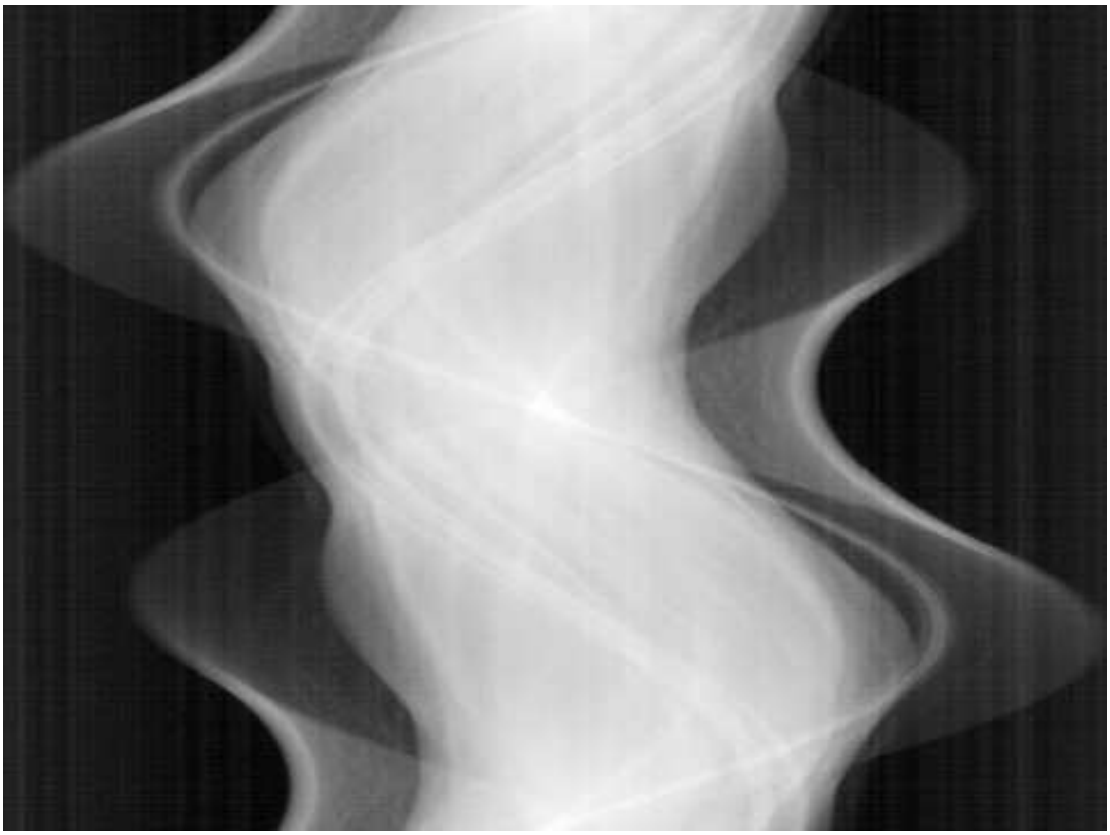

Figure 2.2. Fanbeam sinogram of a mouse

the photon to the electron. Most importantly for CT imaging, both of these effects are dependent on the energy of the photon in question. Thus, attenuation is dependent on the photon energy.

An X-ray beam is composed of photons with energies typically ranging between 20 and 150 keV for medical imaging purposes [6]. An X-ray source emits photons with energies in some range, which is dependent on the particular X-ray source. Unfortunately, since the photon energies will be distributed throughout this range, the X-ray beam is polychromatic. Since attenuation is dependent on the photon energy, and the X-ray beam is polychromatic, precise modeling of the process of attenuation is very difficult.

Rather than attempting to model the attenuation in terms of polychromatic X-ray beams, it is often assumed that the X-ray beams are monochromatic, or consisting only of photons with equivalent energies. With this assumption, the model for attenuation in the three dimensional case simplifies to [6]

$$N_d = N_0 \exp\left\{-\int_{ray} \mu(x,y,z)ds\right\} \tag{2.3}$$

where N_0 is the number of photons emitted from the source, N_d is the number of photons received at a detector cell, ray is the path joining the source and the detector cell, and $\mu(x,y,z)$ is the attenuation map of the object at location (x,y,z). Furthermore, we can rewrite equation (2.3) as

$$\int_{ray} \mu(x,y,z)ds = \ln\frac{N_0}{N_d}. \tag{2.4}$$

Comparing this to (2.1), it is evident that the line integral values are specified by the right hand side of (2.4). Note that the N_0 and N_d values will be known and that the ray path can be approximated, so $\ln(N_0/N_d)$ yields an approximation to the line integral of $\mu(x, y, z)$ along the path described by ray.

Although the assumption of monochromatic X-ray energies simplifies the model for attenuation, it can lead to artifacts in the reconstructions. Since objects tend to attenuate lower energy photons more readily than higher energy photons, the effective energy level of the X-ray beam is increased when passing through an object. This phenomenon is known as beam hardening and leads to two primary reconstruction artifacts [6]. The first involves artificially high attenuation coefficients near the perimeter of highly attenuating objects, such as bone. The second involves streaks near highly attenuating objects. Researchers have proposed several techniques for eliminating the beam hardening effects, but none are examined in this thesis.

Furthermore, although the preceding descriptions of the projection data are based on line integrals, they do not accurately describe the geometry of a real scanner. Since each detector cell has some area associated with it, the recorded photons travelled through some three dimensional volume of the object rather than along a single line before reaching the detector. We consider this discrepency when designing the system models later in this chapter. Note that although the reading at a particular detector cell involves some three dimensional path through the object, we refer to these paths as projection rays throughout this thesis.

2.2 Representation as a Linear System

Let the object to be reconstructed be represented by $f(x, y, z)$. Discretize this image as a collection of N volumetric picture elements, or voxels, each of constant value. This collection of voxels approximates the attenuation map of the object, and can be represented in vector form as $\mu = (\mu_1, \mu_2, \ldots, \mu_N)$. For the jth voxel, let μ_j represent the constant value of the voxel. The goal of the reconstruction is now to assign values to each of the voxels such that they approximate the true attenuation map as closely as possible.

The data available to perform the reconstruction is the geometry and settings of the scanner and the M projection readings. These projection readings originally take the form of photon counts as indicated in equation (2.3), but we modify them to take the form of equation (2.4). Let p_i represent the ith such projection ray and let $p = (p_1, p_2, \ldots, p_M)$ represent the collection of all projection rays over all view angles.

Relating the projection space to the voxel space requires the formation of a system matrix, A, that accounts for the geometry of the scanner, modeling of the process of attenuation, collimation, detector response, etc. This system matrix will have MxN entries where a_{ij} quantifies the effect of the jth voxel on the attenuation of the ith projection ray. Thus, the product $A\mu$ translates from the voxel space to the projection space, and $A^T p$ translates from the projection space to the voxel space. These operations are known as forward projection and backprojection, respectively. Determining the values of the system matrix plays a critical role in the reconstruction process and is

considered further in section 2.3.

Using the above terminology, we express the image reconstruction problem as the linear system

$$A\mu + s = p \tag{2.5}$$

where s accounts for scatter and other types of additive noise and distortion. For the purposes of this thesis, we only model the scanner geometry and the process of attenuation, so s is assumed to be zero. Given this system, we can apply various techniques for solving linear systems to approximate the attenuation map of the object. Note, however, that p typically includes noise and that μ is subject to a nonnegativity constraint since a negative value would physically correspond to a portion of the object that increases rather than decreases the number of photons in the X-ray. These facts should be considered when choosing a reconstruction algorithm. Several reconstruction algorithms are presented in chapter 3.

2.3 Modeling Techniques

The quality of the system matrix A has a substantial impact on the accuracy of the reconstruction. Although ideally the entry a_{ij} should fully quantify the effect of voxel j on projection ray i, creating a matrix of this form is seemingly computationally prohibitive. Thus, we pursue techniques to acceptably approximate these ideal values in a

computationally feasible fashion.

2.3.1 Ideal Model

Consider the transmission energy that is collected at a single detector cell. To determine the path through which the X-rays traveled to reach this detector, connect the perimeter of the detector cell back to the X-ray source to form the contributing volume. Now, the entry a_{ij} is the volume of the intersection between voxel j and the path corresponding to the ith projection ray.

Note that even the above includes simplification of the scanner geometry. In reality, the source is not a point source. Rather, it has some nonzero area. However, finding the volumes to fit even the slightly simplified model above is a significant computational burden. Doing so would involve finding the volumetric intersection of a three dimensional path with a potentially large set of voxels. This operation would have to be repeated for each detector cell and for each view angle.

Fortunately, there are simplified techniques for constructing the system matrix which produce acceptable results with much more manageable computational requirements.

2.3.2 Single Line Intersection Model

Rather than the entire three dimensional path, consider only the line which joins the X-ray source to some point in the detector cell, such as the center of the detector cell. Computing the intersection of this sample line with each voxel yields a rough approximation of that voxel's contribution to the attenuation of the energy collected

at the detector cell. This is depicted in figure 2.3 where w_j denotes the length of the intersection with the jth voxel. Note, however, that the consideration of only one line will not include all of the voxels that actually contributed to the attenuation of the energy collected at the detector cell since a single line cannot represent the full volume of a given path. Additionally, the relative weights of each voxel will not be the same as in the ideal case, which further compromises the validity of a single line based model.

The attractive aspect of this modeling approach is the computational ease of finding the line intersections. An efficient method of computing these intersections was proposed by Siddon [13] and later improved by Jacobs et al. [5]. The basic premise of the fast radiological path calculation involves iteratively stepping along the projection ray, which is represented parametrically, to find each of the intersection points with the pixel or voxel space. First, represent the projection ray as

$$p = s + \alpha(d - s) \tag{2.6}$$

where p is some point along the line, s is the source point, and d is the destination point. Each of p, s, and d is a vector containing the x, y, and z coordinates of the points in the three dimensional scanner coordinate system. We first calculate the α values corresponding to entering and exiting the voxel space. We then calculate the number of x, y, and z planes intersected by this line in the voxel space. Based on this information, we can iteratively step through the α values corresponding to intersections with the voxels and calculate the distances associated with these intersections.

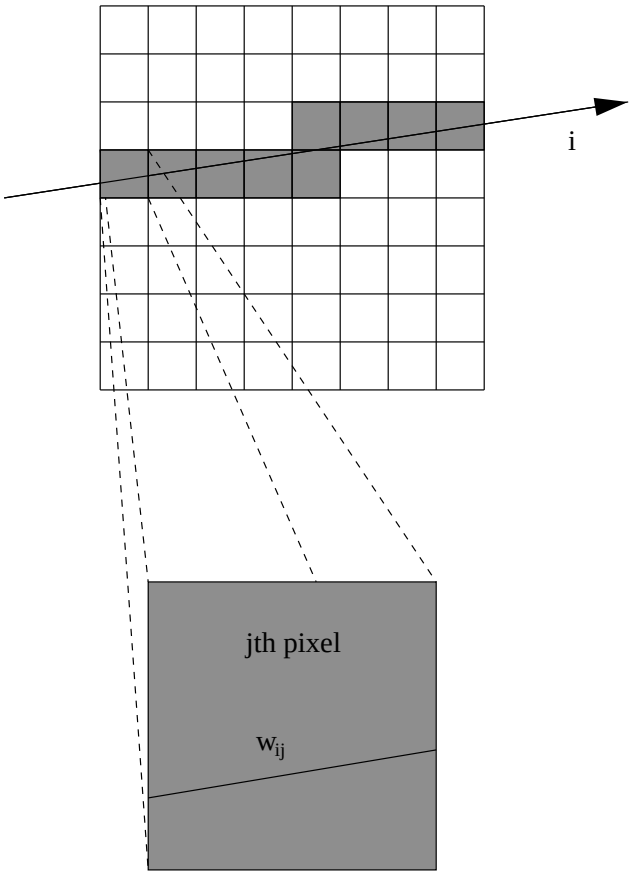

Figure 2.3. Line intersections with pixels

Unfortunately, the use of line intersections yields serious artifacts in the reconstructions. The most significant of these artifacts takes the form of rings in the reconstructed images. These are due to interference patterns emerging from the conebeam geometry. We analyze the causes and effects of these artifacts more thoroughly in the results section. This phenomenon was previously noted and explained by Zeng and Gullberg [16].

2.3.3 Multiple Line Based Model

One method of mitigating the ring artifacts produced by the single line based models is using multiple sample lines per detector cell rather than a single line. After computing the line intersections for each of the chosen lines, the intersection values for each voxel can be averaged to yield a single row in the system matrix.

Assuming the sample lines are chosen in a reasonable fashion, the likelihood of including each voxel that contributed to the attenuation of a given ray grows as the number of sample lines increases. Furthermore, the relative weights for each voxel should approach the true values as the number of sample lines increases. Thus, the quality of the system model should increase as the number of sample lines increases. Of course, the computational burden of computing the system matrix also increases with the number of sample lines. The results section includes a more quantitative analysis of the multiple line based model using varying number of lines per detector cell.

2.3.4 Trilinear Interpolation Model

The trilinear interpolation model is based upon a significantly different approach than the volume or line based techniques mentioned in the above sections. The following development is the three dimensional equivalent of the two dimensional interpolation based scheme introduced in [6]. The general idea of the trilinear interpolation model is to segment the projection ray into points, calculate the relative contributions of the eight closest voxel centers to each of these points, and sum the contributions to approximate the system matrix values. Note that the physical interpretation of these values is not as clear as the line intersection based models. This causes some data scaling issues that we address in the results section.

To more formally specify the trilinear interpolation model, first express the relationship between the attenuation map $\mu(x, y, z)$ and the projection data as

$$p_i = R_i\mu(x, y, z) = \int_{-\infty}^{\infty}\int_{-\infty}^{\infty}\int_{-\infty}^{\infty} \mu(x, y, z)\delta(r_i(x, y, z))\, dx\, dy\, dz \tag{2.7}$$

where $r_i(x, y, z) = 0$ represents the equation of the ith ray and R_i is the projection operator along the ith ray. The goal is to approximate the true attenuation map $\mu(x, y, z)$ as closely as possible with a discretized attenuation map. This discrete attenuation map requires a choice of basis functions $b_j(x, y, z)$.

Assume the basis functions are chosen and using N of them yields an acceptable

approximation to $\mu(x, y, z)$. Based on these assumptions, we have

$$\mu(x, y, z) \approx \sum_{j=1}^{N} g_j b_j(x, y, z) \tag{2.8}$$

where g_j's are the coefficients of expansion representing $\mu(x, y, z)$ relative to the basis set $b_j(x, y, z)$. Using substitution, the forward projection process can be written as

$$p_i = R_i\mu(x, y, z) \approx \sum_{j=1}^{N} g_j R_i b_j(x, y, z) = \sum_{j=1}^{N} a_{ij} g_j \tag{2.9}$$

where a_{ij} represents the line integral of $b_j(x, y, z)$ along the ith ray. Note that if a pixel basis is chosen for $b_j(x, y, z)$, this model simplifies to the line intersection based approach above.

However, for the trilinear interpolation approach, trilinear basis elements are chosen instead. These basis functions offer support over eight voxels. We approximate the ray integral over $R_i\mu(x, y, z)$ by a finite sum over a set of M_i equidistant points $\mu(s_{im})$, for $1 \leq m \leq M_i$, by

$$p_i \approx \sum_{m=1}^{M_i} \mu(s_{im})\Delta_s \tag{2.10}$$

where Δ_s is a step size and $\mu(s_{im})$ is calculated from the values g_j of $\mu(x, y, z)$ on the

eight nearest voxels centers by trilinear interpolation. We write this as

$$\hat{f}(s_{im}) = \sum_{j=1}^{N} d_{ijm} g_j \tag{2.11}$$

for $m = 1, 2, \cdots, M_i$. Thus, d_{ijm} is the contribution of the jth voxel to the mth point on the ith ray. Substituting (2.11) into (2.10) yields

$$p_i = \sum_{m=1}^{m_i} \sum_{j=1}^{N} d_{ijm} g_j \Delta_s = \sum_{j=1}^{N} a_{ij} g_j \tag{2.12}$$

where the coefficients a_{ij} are defined as the sum of the contributions by the jth voxel to the ith ray along all of the sample points of the ray. Thus,

$$a_{ij} = \sum_{m=1}^{M_i} d_{ijm} \Delta_s. \tag{2.13}$$

In the present implementation, we store the a_{ij} values from equation (2.13) in the system matrix. Furthermore, we choose equidistant sample points along the line connecting the X-ray source to the center of a given detector cell and set the step size, Δ_s, to half the width of a voxel as recommended by Kak and Slaney [6]. We can then use the resulting system matrix just as we would for the single and multiple line intersection models.

One aspect of the trilinear interpolation technique worthy of note is that some voxels that made no contribution to the attenuation of a given ray may be included

as a contributing voxel for that ray. This could occur when one or more of the eight neighboring voxel centers of a sample point $\mu(s_{im})$ corresponds to a noncontributing voxel. In these cases, a smoothing or blurring of the reconstructed image will occur, although it is difficult to quantify the extent of this blurring. Also, this side effect may be desirable.

Chapter 3

Survey of Algorithms

We can subdivide the class of iterative algorithms used for image reconstruction into algebraic and statistical algorithms. From the class of algebraic reconstruction algorithms, we chose to implement the Simultaneous Algebraic Reconstruction Technique (SART) [6]. The statistical algorithms implemented include Expectation Maximization (EM) [12], [7] and a Weighted Least Squares (FWLS) reconstruction technique proposed by Fessler [2]. We present each of these algorithms in this chapter.

3.1 Algebraic Reconstruction Techniques

The only algebraic reconstruction algorithm implemented in this thesis is SART, although several others exist, such as the Algebraic Reconstruction Technique (ART) and the Simultaneous Iterative Reconstruction Technique (SIRT). Of these three, however, SART is the most sophisticated and fits nicely into the developed framework.

3.1.1 Algebraic Reconstruction Preliminaries

This development of the algebraic reconstruction techniques follows closely from the appropriate material in [6]. Recall from section 2.2 that we can express the reconstruction problem as the linear system

$$A\mu = p, \tag{3.1}$$

where a_{ij} is the contribution of the jth voxel to the attenuation of the ith projection ray, μ_j is the value of the jth voxel, and p_i is the ith projection ray. We compute the system matrix A using the techniques discussed in chapter 2.

Assume that p contains M projection rays and μ contains N voxels. Therefore, the image represented by μ is a point in an N-dimensional voxel space and the M equations described by the linear system represent hyperplanes in this voxel space. If a unique solution to the linear system exists, then these hyperplanes intersect at a single point in the voxel space that represents this unique solution. However, since the system is generally over determined ($M > N$) or underdetermined ($M < N$) and noise is included in the projection data, the linear system does not contain a unique solution. Thus, we must consider convergence properties for proposed algebraic reconstruction algorithms.

The technique at the heart of the algebraic reconstruction algorithms is the "method of projections" introduced by Kaczmarz. First, take an initial guess,

$$\mu^{(0)} = (\mu_1^{(0)}, \mu_2^{(0)}, \cdots, \mu_N^{(0)}), \tag{3.2}$$

where μ represents one point in the N-dimensional voxel space. Project this guess onto the first hyperplane described in the linear system, then reproject the resultant point onto the second hyperplane described by the linear system, and so on. Projecting onto the Mth hyperplane completes the first iteration and this process is continued until the solution is acceptable. We can mathematically describe this process by

$$\mu^{(i)} = \mu^{(i-1)} + \frac{(p_i - \mu^{(i-1)} \cdot a_i)}{a_i \cdot a_i} a_i \tag{3.3}$$

where $\mu^{(i)}$ is the approximation after performing i projections, $\cdot$ represents a dot product, and a_i is the ith row of A, or $a_i = (a_{i1}, a_{i2}, \cdots, a_{iN})$. Note that M projections are required to complete a full iteration, so kM projections are required for k iterations.

If a unique solution exists, this series of projections is guaranteed to converge to the solution. It has been shown that in the case of an overdetermined system, the approximated solutions will oscillate around the neighborhood of the intersections of the hyperplanes. Furthermore, it has also been shown that in the case of an underdetermined system, (3.3) converges to a solution, f', that minimizes $|f^{(0)} - f'|$.

3.1.2 SART

The Simultaneous Algebraic Reconstruction Technique (SART) includes a modification to the update equation that allows an averaged voxel update after all of the projections are considered rather than after each projection ray. Since we implemented the algorithms using the Message Passing Interface (MPI) for parallel load distribution, the

aggregated update technique is highly advantageous as it requires less communication overhead. Furthermore, we can implement the aggregate updates using forward and backprojections of the system matrix which fits nicely into the developed framework. The alternate update technique used in SART yields the following update for each voxel after the kth iteration:

$$\mu_j^{(k+1)} = \mu_j^{(k)} + \frac{\sum_i \left[a_{ij} \frac{p_i - a_i \cdot \mu^{(k)}}{\sum_j a_{ij}} \right]}{\sum_i a_{ij}}. \tag{3.4}$$

To be used in the current framework, we need to express this algorithm in terms of a linear system using forward and backprojections. Let vectors R and C represent the row and column sums of A, respectively, so $R_i = \sum_j a_{ij}$ and $C_j = \sum_i a_{ij}$. Then we can express equation (3.4) as

$$\mu^{k+1} = \mu^k + \{A^T[(p - A\mu^k) \oslash R]\} \oslash C \tag{3.5}$$

where $\oslash$ represents element-wise division. Thus, each iteration of SART requires one forward projection and one backprojection.

One additional modification proposed for SART is the heuristic application of a Hamming window to each projection ray. The inclusion of the Hamming window emphasizes the central portions of each projection ray and has been experimentally shown to improve the reconstruction quality. However, including the Hamming window yields a proliferation in the number of elements that must be stored. Thus, since storage is a

major consideration for the iterative framework, we did not employ a Hamming window modification.

3.2 Statistical Reconstruction Techniques

The class of statistical reconstruction techniques covered in this thesis includes Expectation Maximization (EM) and a Weighted Least Squares (FWLS) reconstruction algorithm. Whereas the algebraic techniques evolve directly from an algebraic interpretation to a linear system, the statistical techniques are founded in a statistical context with solution techniques representable as a linear system.

3.2.1 Expectation Maximization

The expectation maximization (EM) algorithm for emission tomography was proposed by Shepp and Vardi [12]. Shortly thereafter, it was independently proposed by Lange and Carson, who extended it to transmission tomography [7]. Previous to the work related to computed tomography, an EM algorithm was proposed by Richardson [11] and Lucy [8] for use in the realm of astronomy.

For the purposes of this thesis, we implement the emission EM algorithm rather than the transmission algorithm. This is due to the relative ease with which the emission algorithm fits into the linear system based framework that we have developed. On the other hand, the implementation of the transmission algorithm using the linear system framework is seemingly more difficult. In particular, the transmission model

introduces a proliferation of new variables which cannot be modeled using forward and backprojections. Usage of the emission EM algorithm for transmission reconstruction is also documented by Wang in [15]. The following development follows closely to the development in [7].

The goal of emission CT is to approximate the photon emission intensities of some object. As with transmission CT, the object is represented as a collection of voxels. Let λ_j denote the average source intensity for voxel j and b_{ij} represent the probability that a photon leaving voxel j reaches the ith projection detector. Furthermore, let Δt_i denote the length of the aquisition time for projection i and let $c_{ij} = b_{ij}\Delta t_i$. Note the similarities between the λ_j and c_{ij} quantities in the emission case and the μ_j and a_{ij} values in transmission case.

Let X_{ij} be the random number of photons that are emitted by voxel j and contribute to projection i. Then the mean of X_{ij} is $c_{ij}\lambda_j$. Furthermore, let Y_i represent the total number of photons recorded for the ith projection. Thus,

$$Y_i = \sum_j X_{ij}. \tag{3.6}$$

As shown in [7], X_{ij} and Y_i are both Poisson distributions. The Y_i values represent the recorded data and are shown above to be functions of the X_{ij} data values. Thus, X_{ij} represents a complete but unobserved set of data from which Y_i can be derived.

The EM algorithm works by increasing the log likelihood of the observed data with respect to the current estimation of the source intensity values at each iterative step.

This process involves two steps: an E-step, which forms a conditional expectation, and an M-step, which involves maximizing the conditional expectation to give new source intensity estimations.

Using the above definitions, the E-step can be formulated as

$$E(\ln f(X,\lambda)|Y,\lambda^n) = \sum_i \sum_j \{-c_{ij}\lambda_j + N_{ij} ln(c_{ij}\lambda_j)\} + R, \tag{3.7}$$

where $f(X,\lambda)$ is the density function of X, λ^n is the current estimation of the source intensity values, R is independent of the new λ, and N_{ij} is given by

$$N_{ij} = E(X_{ij}|Y_i,\lambda^n) = \frac{c_{ij}\lambda_j^n Y_i}{\sum_k c_{ik}\lambda_k^n}. \tag{3.8}$$

The M-step is implemented by taking the partial derivatives of (3.8) with respect to λ_j, setting them to zero, and solving to get the following update equation:

$$\lambda_j^{n+1} = \frac{\lambda_j^n}{\sum_i c_{ij}} \sum_i \frac{c_{ij} Y_i}{\sum_k c_{ik}\lambda_k^n}. \tag{3.9}$$

Note that if the initial source intensity estimation, λ^0, is nonnegative in (3.9), then each subsequent λ^n will be nonnegative as well. This is a highly desirable feature of the EM algorithm as the physical aspect of attenuation, or source intensity in the emission case, imposes a non-negativity constraint on a reasonable solution.

In order to use update equation (3.9) in the current framework, it must be stated

in terms of a linear system using forward and backprojection operations. To do this, let $C = [c_{ij}]$, $\lambda = [\lambda_j]$, and $Y = [Y_i]$. The scaling factor represented by $\sum_i c_{ij}$ is simply a vector of column sums that can be computed by backprojecting C over a vector of ones. Denote this set of column sums as S. The term

$$\sum_i \frac{c_{ij} Y_i}{\sum_k c_{ik} \lambda_k^n} \tag{3.10}$$

is equivalent to $C^T(Y \oslash C\lambda^n)$ where $\oslash$ represents element-wise division and matrix multiplication has the highest priority in the order of operations. Thus, the entire update algorithm can be stated as

$$\lambda^{n+1} = (\lambda^n \otimes C^T(Y \oslash C\lambda^n)) \oslash S \tag{3.11}$$

where $\otimes$ and $\oslash$ represent element-wise operations as before.

However, (3.11) is still in terms of the emission case. To use this for the transmission case, replace C, λ, and Y by A, μ, and p, respectively. Recall that $A = [a_{ij}]$ represents the effect of voxel j on the attenuation of projection ray i, $\mu = [\mu_j]$ is the attenuation coefficient of voxel j, and $p = [p_i]$ is the detector reading for projection ray i. Note that while this development of EM does not directly model the transmission case, the interpretations of the substituted and original values are similar in each case.

Using these substitutions, the EM algorithm used in this thesis is given by

$$\mu^{n+1} = (\mu^n \otimes A^T(p \oslash A\mu^n)) \oslash S \tag{3.12}$$

where S_j is now $\sum_i a_{ij}$.

3.2.2 Weighted Least Squares

The last reconstruction technique implemented for this thesis is a Weighted Least Squares (FWLS) technique described by Fessler [2]. The following presentation mimics that development closely. As presented, this model assumes that the X-ray beams are monoenergetic. In the referenced paper, this model was extended to work with polyenergetic X-ray beams, but that work was not implemented in this thesis.

Recall from equation (2.3) that attenuation in the monoenergetic case can be represented by

$$N_d = N_0 \exp\left\{-\int_{ray} \mu(x,y,z)ds\right\} \tag{3.13}$$

where N_0 is the source energy, $\mu(x,y,z)$ is the attenuation map for the object, ray is some projection ray, and N_d is the resultant energy after attenuation. For notational convenience, we rewrite this equation as

$$Y_i = I_i \exp\left\{-\int_{L_i} \mu(x,y,z)ds\right\} \tag{3.14}$$

where Y_i is now interpreted as the detector reading for the ith projection ray, I_i is the source energy for the i projection ray, and L_i is the path of the ith projection ray.

Now, assume the following statistical model for the projection measurements:

$$p_i \sim \text{Poisson}\{b_i \exp^{-[Af]_i} + r_i\}, \quad i = 1, \ldots, N \tag{3.15}$$

where b_i is the blank scan factor, r_i is a noise correction factor accounting for background events and projection read-out noise variance, A is the system matrix discussed in chapter 2, $[Af]_i = \sum_{j=1}^{p} a_{ij} f_j$ is the ith line integral, and N is the number of measured rays. We determine the blank scan factor values by performing a partial scan with no objects located in the scanner. These values can then be used as a close approximation to the I_i values in equation (3.14). We determine the noise correction factor by performing a scan with the X-ray source blocked to determine a baseline reading for the scanner environment. Thus, the a_{ij}, b_i, and r_i values are all known before commencing the reconstruction.

The reconstructed image, f, can be approximated by maximizing the following Poisson log-likelihood:

$$L(f) = \sum_{i=1}^{N} \{Y_i \, log(b_i e^{-[Af]_i} + r_i) - (b_i e^{-[Af]_i} + r_i)\}. \tag{3.16}$$

To help prevent noisy data from yielding a poor reconstruction, a regularization term can be added to (3.16) to enforce a known structure of the object on the reconstructed

image. For example, since adjacent voxels should generally have similar values, the regularization term can penalize differences in the values of neighboring voxels. However, we did not explore penalties in this thesis. Adding a non-negativity constraint, the goal of the reconstruction is now:

$$\hat{f} = \underset{f \geq 0}{\operatorname{argmax}} \; L(f). \tag{3.17}$$

To develop an iterative algorithm, first rewrite (3.16) as

$$-L(f) = \sum_{i=1}^{N} g_i([Af]_i), \tag{3.18}$$

where

$$g_i(l) = -Y_i log(b_i e^{-l} + r_i) + (b_i e^{-l} + r_i). \tag{3.19}$$

Applying a second order Taylor expansion to $g_i(l)$ around an estimate $\hat{l}_i$ of the line integral yields the following approximation:

$$g_i(l) \approx g_i(\hat{l}_i) + g_i'(\hat{l}_i)(l - \hat{l}_i) + \frac{g_i''(\hat{l}_i)}{2}(l - \hat{l}_i)^2. \tag{3.20}$$

Assuming $Y_i > r_i$, the line integral can be estimated as

$$\hat{l}_i = \log(\frac{b_i}{Y_i - r_i}). \tag{3.21}$$

Substituting the estimate for $\hat{l}_i$ into (3.20) yields

$$g_i(l) \approx (Y_i - Y_i \log Y_i) + \frac{w_i}{2}(l - \hat{l}_i)^2 \tag{3.22}$$

where w_i is defined by

$$w_i \quad = \quad \begin{cases} \frac{(Y_i - r_i)^2}{Y_i}, & Y_i > r_i \\ 0, & Y_i \leq r_i. \end{cases} \tag{3.23}$$

Since the first term in (3.22) is independent of l, it can be dropped. Substituting (3.22), with the first term dropped, into (3.18) yields the following FWLS cost function:

$$\text{Ł}(f) = \sum_{i=1}^{N} \frac{w_i}{2}([Af]_i - \hat{l}_i)^2. \tag{3.24}$$

Rather than minimizing $L(f)$, it can be replaced by a surrogate function $\phi(f; f^n)$ that is easier to minimize. The surrogate function chosen in [2] is

$$\phi(f; f^n) = \sum_{i=1}^{N} \sum_{j=1}^{p} \alpha_{ij} \frac{w_i}{2} \left(\frac{a_{ij}}{\alpha_{ij}}(f_j - f_j^n) + [Af^n]_i - \hat{l}_i \right)^2 \tag{3.25}$$

where

$$\alpha_{ij} = \frac{a_{ij}}{\sum_{j=1}^{p} a_{ij}}. \tag{3.26}$$

Setting the first derivative of $\phi(f)$ to zero yields the following update equation:

$$f_j^{n+1} = \left[f_j^n - \frac{\sum_{i=1}^N a_{ij} w_i ([Af^n]_i - \hat{l}_i)}{\sum_{i=1}^N \frac{a_{ij}^2 w_i}{\alpha_{ij}}} \right]_+, \quad j = 1, \ldots, p, \tag{3.27}$$

where $[]_+$ enforces nonnegativity by setting f_j^{n+1} to zero if the above equation produces a negative number.

In our implementation, μ and p are substituted for f and Y, respectively. While we used our typical forward projector for the line integral approximation, $[Af^n]_i$, we used a specialized backprojector for the backprojection operation due to the extra weighting terms.

Chapter 4

Managing the System Matrix

The most significant hurdles to overcome when implementing the iterative reconstruction algorithms are the potentially massive size of the system matrix and the computational time required to perform operations using the system matrix. One option is to recompute the system matrix values during each iteration rather than storing them. While this approach mitigates the storage requirements, it results in a significant duplication of computation since the system matrix remains the same for each iteration. If many iterations are requested or the system modeling technique is complicated, this could result in a significant increase in total computation time. Thus, instead of pursuing this option, we developed and employed techniques to reduce the storage requirements of the system matrix. We introduce these techniques in the following sections.

4.1 Explicit Storage

The most direct approach for representing the system matrix involves explicitly storing each matrix value. Using this approach would require $P \times D_y \times D_z$ rows and $N_x \times N_y \times N_z$ columns, where P is the number of projection rays, D_y and D_z are the number of detector cells in the y and z directions, respectively, and N_x, N_y, and N_z denote the dimensions of the voxel space in the x, y, and z directions, respectively. Even for a relatively small scanner equipped with a 256×256 detector, operating over 360 projections, and for which we reconstruct a $256 \times 256 \times 256$ volume, explicit storage would require approximately 400 trillion entries. If we use four byte floating point numbers for each entry, the storage requirements would be approximately 1.6 petabytes, or 1600 terabytes. Many scanners have larger detectors, acquire data for more view angles, and require larger image volumes to be reconstructed. Clearly, explicit storage is far too simplistic an approach.

4.2 Sparse Storage

Recall that a nonzero entry a_{ij} in the system matrix denotes that the jth voxel affected the ith projection ray based on a given system model. Thus, with most system models, the vast majority of the entries in the system matrix are zero since a given ray intersects only a small portion of the object. In other words, the system matrix is sparse. While the density of the system matrix depends on the specific modeling technique utilized, it is typically less than 0.001% for the conebeam geometries considered here.

For the purposes of this thesis, we employed the compressed row storage technique for sparse matrix storage [1]. This method requires three vectors: a row pointer vector, a value vector, and a column index vector. Denote these vectors by $\vec{r}$, $\vec{v}$, and $\vec{c}$, respectively. The vectors $\vec{v}$ and $\vec{c}$ each have one entry for every nonzero in the matrix. The vector $\vec{r}$ has size $M + 1$, where M is the number of projection rays. Four byte integers are used for each entry in $\vec{c}$ and $\vec{r}$, and four byte floating point numbers are used for each entry of $\vec{v}$.

Each of the column indices in $\vec{c}$ must encode the i, j, and k indices for a given voxel. We compute the column indices as

$$c = i + jN_x + kN_xN_y \tag{4.1}$$

where c is a column index, and i, j, and k represent the voxel indices in the x, y, and z direction, respectively. We can then recover the original i, j, and k values using

$$i = c \ \% \ N_x \tag{4.2}$$

$$j = (c \ \% \ N_xN_y)/N_x \tag{4.3}$$

$$k = c/(N_xN_y) \tag{4.4}$$

where % denotes the modulo operator and the divisions for j and k are integer divisions. Due to performance issues, we did not perform the column index decoding as above, although our implementation is functionally equivalent. Instead, we take advantage of

the fact that adjacent entries in a row of the matrix often represent adjacent voxels and thus require an update to only a single voxel index. Note that encoding i, j, and k using a four byte integer restricts the voxel space to having a maximum of 2^{32} voxels. While this limit is sufficiently large for the reconstructions performed in this thesis, larger reconstructions would require more voxels, with a corresponding increase in storage requirements.

4.3 System Symmetries

Due to the circular scanning geometry, there are certain symmetries that we can exploit to prevent storing significant portions of the matrix. In fact, exploiting these symmetries reduces the storage requirements by approximately a factor of eight. In the following subsections, we describe the nature of these symmetries for the two dimensional case and then generalize to the three dimensional case.

4.3.1 Overview of Symmetries

The basis of the symmetries can be explained rather simply for the continuous case. The X-ray source follows a circular path around the object as it generates projections. This scanning circle can be subdivided into eight octants as shown in figure 4.1. By reflecting a projection ray from octant one, say $\overline{SD}$, to each of the remaining octants, we generate several additional projection rays that are symmetric to $\overline{SD}$. These symmetric projection rays are depicted in figure 4.2. Thus, by storing only the portion of the system

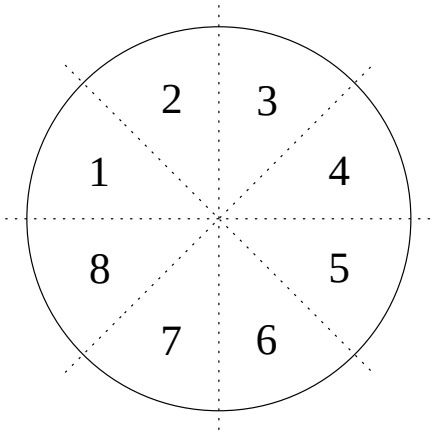

Figure 4.1. Scanning circle octants.

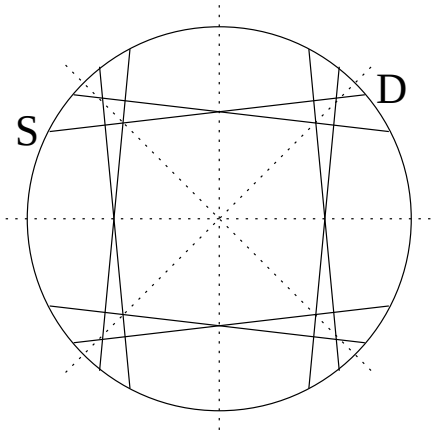

Figure 4.2. All symmetries of $\overline{SD}$.

matrix corresponding to the projection rays originating in octant one, we can generate the corresponding projection rays for the remaining seven octants. This significantly reduces the storage requirements for the system matrix.

4.3.2 Mathematical Formulation of Symmetries

Consider a scanning circle with radius r that is centered at the origin of the coordinate system. Let the X-ray source, S, lie at some point (x, y) along the first octant of the scanning circle. Then a projection ray emitted from S will intersect some other point on the scanning circle, say $D = (x', y')$. This is depicted in figure 4.3. Now, reflect the line segment $\overline{SD}$ about the line $y = -x$, which separates the first and second octants of the scanning circle. The points S and D reflect to $S' = (-y, -x)$ and $D' = (-y', -x')$, respectively. This is illustrated in figure 4.4. Continuing this procedure to get sources in each of the eight octants yields the lines shown in figure 4.2.

In order to relate these observations to the fan beam scanner geometry, it is useful

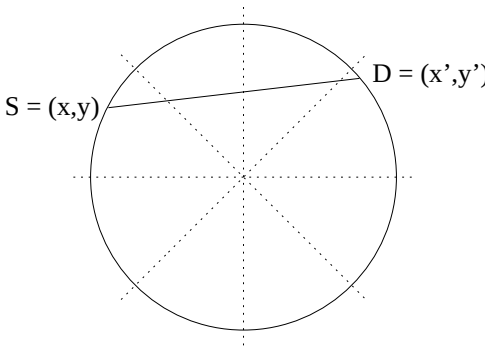

Figure 4.3. Projection ray $\overline{SD}$ (points).

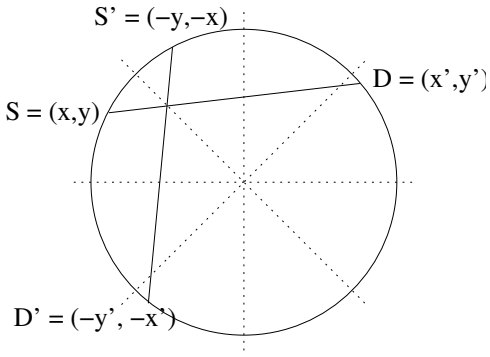

Figure 4.4. Reflection of $\overline{SD}$ (points).

to represent the line segment $\overline{SD}$ in terms of a view angle and fan angle. Label the line connecting the X-ray source to the origin as $\overline{SO}$. Then the view angle, θ, of projection source S is simply the angle between the negative x-axis and $\overline{SO}$. Furthermore, the fan angle, ϕ, is the angle between $\overline{SD}$ and $\overline{SO}$. We illustrate these angles in figure 4.5. Performing the same reflection operation as before yields $\overline{S'D'}$ with view angle θ' and fan angle ϕ' as shown in figure 4.6. It can be easily verified using similar triangles that $\theta' = \pi/2 - \theta$ and $\phi' = -\phi$.

We introduce the notation $l_1 = (\theta, \phi)$ to denote a projection ray, l_1, with view angle θ and fan angle ϕ. We have shown above that reflecting $l_1 = (\theta, \phi)$ about the line $y = -x$ yields $l_2 = (\pi/2 - \theta, -\phi)$. These two lines are symmetric in the sense that we can generate one using the other. Continuing the process of reflection to generate projection rays in each of the eight octants yields the results summarized in table 4.1.

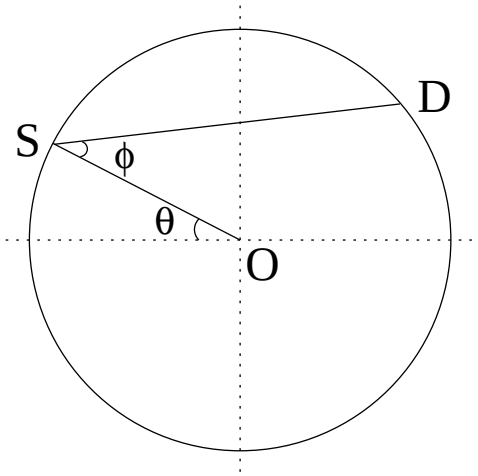

Figure 4.5. Projection ray $\overline{SD}$ (angles).

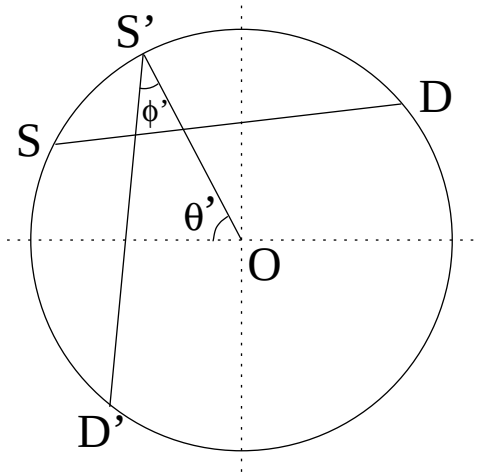

Figure 4.6. Reflection of $\overline{SD}$ (angles).

Table 4.1

Symmetries based on reflection

Line before reflection	Reflected about	Line after reflection
$l_1 = (\theta, \phi)$	$y = -x$	$l_2 = (\pi/2 - \theta, -\phi)$
$l_2 = (\pi/2 - \theta, -\phi)$	$x = 0$	$l_3 = (\pi/2 + \theta, \phi)$
$l_3 = (\pi/2 + \theta, \phi$	$y = x$	$l_4 = (\pi - \theta, -\phi)$
$l_4 = (\pi - \theta, -\phi)$	$y = 0$	$l_5 = (\pi + \theta, \phi)$
$l_5 = (\pi + \theta, \phi)$	$y = -x$	$l_6 = (3\pi/4 - \theta, -\phi)$
$l_6 = (3\pi/4 - \theta, -\phi)$	$x = 0$	$l_7 = (3\pi/4 + \theta, \phi)$
$l_7 = (3\pi/4 + \theta, \phi)$	$y = x$	$l_8 = (2\pi - \theta, -\phi)$

4.3.3 Limitations of Symmetries

Unfortunately, the usage of symmetries imposes some restrictions on the scanner settings and geometry. The first restriction is that projection angles must be distributed such that any angle not in the first octant has an angle symmetric to it in the first octant. The second is that the detector must be centered about the line connecting the X-ray source to the axis of rotation. In other words, the detector cannot have an offset associated with it.

The first restriction is easily overcome by specifying the scanning parameters such that no inconsistencies occur. Choosing view angles that uniformly divide the scanning circle accomplishes this. The second restriction is difficult to prevent at the hardware level, but we can process the acquired projection data to compensate for the offset. In this work, we use linear interpolation to rebin the data such that it satisfies the above centering constraint. This involves ignoring some of the data from the edges of the detector, but allows us to employ the symmetry techniques.

While not a limitation, it should also be noted that the projections corresponding to $\theta = 0$ and $\theta = \pi/4$ are special cases. Each of those projections can only be reflected to yield projection rays for three additional projections rather than seven. For example, $\theta = 0$ is only symmetric to $\pi/2$, π, and $3\pi/2$. Since $\theta = 0$ is not symmetric to $\theta = \pi/4$ by reflection about any of the lines given above, both projections must be stored if in the original projection data set. Therefore, assuming that 360 projections are taken uniformly over the scanning circle, data for the first 46 projections must be stored,

yielding a reduction in storage by nearly a factor of 8.

4.3.4 Implementation of Symmetries

We will now associate these observations regarding symmetries with the storage of values in the system matrix. Assume that the line intersection based system described in section 2.3.2 is implemented for the two dimensional case. First, the area inside the scanning circle is divided into a grid of pixels, which is centered about the origin. The row of the system matrix corresponding to some line segment with its source in the first octant, say l_1, would contain the length of intersection of l_1 with each pixel. Since the pixel grid is centered and reflection maintains length, two intersection points of one pixel will reflect to two intersection points of another pixel, and the length between those points will be identical. Thus, a symmetric projection ray has identical intersection lengths with the pixel grid as l_1. Once determining the mapping of pixel indices that must be carried out during reflection, we can compute the full system matrix by storing only the portion where the X-ray source lies in the first octant. Therefore, by storing only a small subset of the system matrix, we compute the entire system matrix without recalculating the intersection values. Note that since these are three dimensional reconstructions, we use voxels instead of pixels, but the concept remains the same.

More generically, a row in the system matrix is a collection of weights corresponding to the contribution of a particular voxel to the attenuation of a projection ray. Each of these values has an index from which we can determine the three voxel indices i, j, and

k, that correspond to the x, y, and z directions, respectively. We offered one potential implementation of this index decoding in (4.2).

The voxel space has dimensions N_x, N_y, and N_z in the x, y, and z directions, respectively, and indexing for the voxels begins at zero. Thus, for example, possible i values are $0, 1, \ldots, N_x - 1$. Given a row of indices, generating the matrix row for a ray that is symmetric to the given row simply involves changing the voxel indices based on the octant containing the source of the symmetric ray. These voxel index changes are given in table 4.2. This table gives the conversion for voxel indices (i, j, k) corresponding to a projection ray with its source in octant one to voxel indices (i', j', k') corresponding to a symmetric projection ray.

This allows for the following implementation. We store the intersection data for any projection ray that has the X-ray source in the first octant of the scanning circle. We also provide a method to request a specific row of the matrix, which may or may not be stored. If the row is stored, we simply return it. Otherwise, we determine the row that represents the ray in the first octant symmetric to the row being requested. We can then construct the requested matrix row from the stored row by the given index changes and return it to the caller. To improve the efficiency of these operations, we compute and use all of the projection rays symmetric to a given ray at the same time. Otherwise, we must decode the column indices for the stored rays more than is necessary.

Table 4.2

Voxel index updates for symmetries

Octant	Resulting voxel indices
1	$(i', j', k') = (i, j, k)$
2	$(i', j', k') = (N_y - 1 - j, N_x - 1 - i, k)$
3	$(i', j', k') = (j, N_x - 1 - i, k)$
4	$(i', j', k') = (N_x - 1 - i, j, k)$
5	$(i', j', k') = (N_x - 1 - i, N_y - 1 - j, k)$
6	$(i', j', k') = (j, i, k)$
7	$(i', j', k') = (N_x - j - 1, i, k)$
8	$(i', j', k') = (i, N_x - j - 1, k)$

4.4 Disk storage

Despite the efforts in the previous sections to reduce the memory requirements of the system matrix, larger reconstructions still command significant storage requirements. To handle these cases, we allow storing the system matrix to disk so that the reconstruction software can read and use managable sized sections of the matrix on demand. Note that this approach introduces the option of generating and storing the matrix well before the reconstruction begins and thus avoiding that overhead during the reconstruction. Furthermore, if the resolution requirements of the reconstruction remain constant for several reconstructions, we can use the same system matrix for each reconstruction, assuming that the scanner geometry does not change. Therefore, we can also employ this technique on smaller reconstructions to avoid the overhead involved in creating the system matrix. In these smaller cases, we simply read the entire system matrix from disk and store it in main memory.

To obtain better performance, we only write the data for the projections with sources

in the first octant of the scanning circle to disk. We compute the remaining data using the system symmetries. Furthermore, by using two threads to perform these operations, the system naturally staggers itself such that one thread can be interpreting and using the data while another reads data from the disk. After completing their respective tasks, these threads switch roles. This implementation reduces the ultimate impact on performance. We include timing information regarding the impact of the disk reads in the results section.

4.5 Implementation Issues

4.5.1 Spherical Support Region

A scanner provides data support for some location if projection data is available for that location for some view angle. Recall that the conebeam geometry emits X-rays from the source in a cone shape as it rotates around the scanning circle. Intersecting the cones over all possible view angles yields a spherical region in the scanning area for which the scanner provides full data support. We refer to this region as the spherical support region (SSR). Since voxels located outside of the SSR lack full data support, we do not include them in the system matrix. This prevents unnecessarily allocating storage or computational resources to reconstruct these voxels.

4.5.2 Multi-Threading

Since we typically run the reconstructions on machines with more than one processor, being able to harness the additional processors is advantageous. In this project, we distribute both the forward and backprojectors across the available processors using POSIX threads. This distribution is accomplished by simply assigning to each of the n processors $1/n$ of the data available for each projection.

4.5.3 Load Distribution via MPI

Due to the potential size and computational burden of the presented iterative reconstruction procedures, it is highly beneficial to distribute the storage and computational requirements to a cluster of machines. We perform this distribution using the LAM/MPI implementation version 6.5.8.

Distributing the System Matrix

Since the total storage requirements are dominated by the system matrix, the largest storage savings will result from distributing this system matrix as equally as possible across all of the cluster nodes. We accomplish this by assigning certain projections to each node. First, we determine the total number of projections to store based on the number of view angles and the symmetry setting. If the number of MPI hosts evenly divides the number of projections to store, then we assign an equal number of projections to each MPI host. Otherwise, we distribute the projections as equally as

possible, although some hosts will get one more projection than some of the others.

Since the hosts must frequently share data during the iterative reconstructions, which requires all of the hosts to be at an equivalent stage of the computation, an unequal load distribution will force some hosts to wait idly on others. We generally avoided this situation during the test runs by ensuring that the number of MPI hosts evenly divided the number of projections to store.

The implementation of the forward and backprojectors on these partial data sets is straightforward. The pieces of data necessary for the backprojector and forward projector are shown graphically in figures 4.7 and 4.8. As before, A represents the system matrix, μ is the attenuation map of the object, and p is the projection data. The shaded areas depict portions of A, μ, and p which are required for either reading or writing during the forward and backprojections. Note that all of μ is required during a forward projection even when only part of the system matrix is used. This has the consequence that before performing a distributed forward projection, each node must contain a complete copy of the fully up-to-date voxel space values. To achieve this, we coalesce the voxel space data after each backprojection. Note that there is no need to coalesce the data after the forward projections since each node only needs to handle projection space data corresponding to the projections that it stores.

Communication of Results

While the above approach successfully distributes the storage requirements across several MPI hosts, it also necessitates frequent communication during the reconstruction

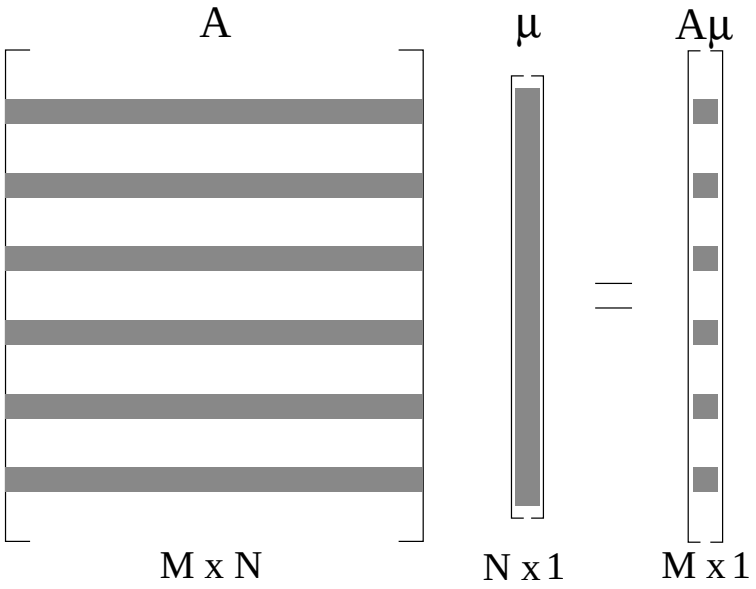

Figure 4.7. Partial forward projection.

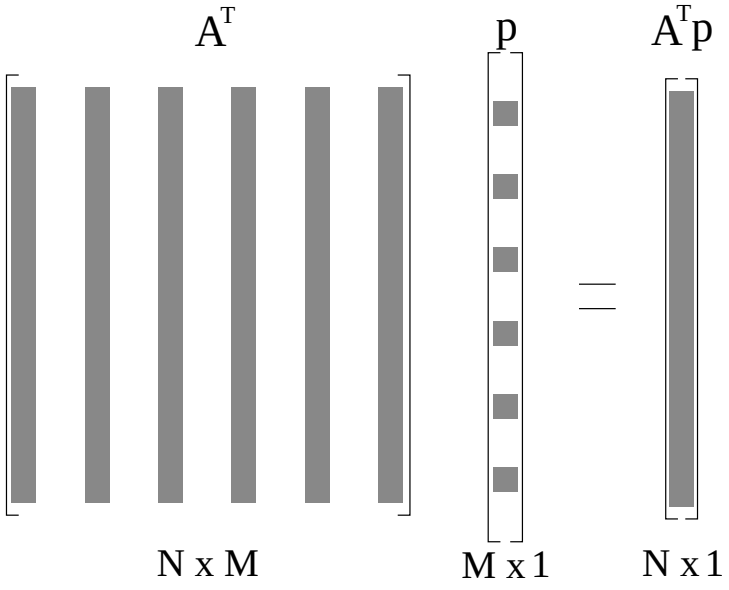

Figure 4.8. Partial backprojection

iterations. However, some of that communication is extraneous. Since a portion of the voxel space will lie outside of the SSR, communicating results for the outlier voxels is unnecessary. In order to increase the performance of the communication after a back-projection, we compact the voxel space before transmission and expand it afterwards. We accomplish this by storing all of the voxels that lie inside the SSR into an array, transmitting that array, and then extracting the data back into the full voxel space. However, since the vast majority of the voxel space is inside the SSR for the geometries that we encountered during this work, this modification only yields slight performance improvements.

Chapter 5

Experimental Results

5.1 Computing Environment

Each of the following reconstructions was performed on a cluster of machines at the University of Tennessee, Knoxville. The cluster consists of 32 nodes running Linux. Each node is equipped with dual Intel XEON Pentium 4 2.4GHz processors, 2GB of RAM, and a Gigabit ethernet card. Since each of our reconstructions involved scans with 360 equally spaced projections, we stored system matrix data for the first 46 projections, which corresponds to the first octant of the scanning circle, and computed the remaining system matrix data based upon symmetries. Thus, we used 23 total cluster nodes, each containing data for two projections. Increasing the number of cluster nodes would not increase performance unless 46 nodes were available since the computation can only proceed as quickly as the slowest node.

5.2 System Model Analysis

Development of the system model involves a tradeoff between accuracy and computational efficiency. The model needs to be accurate enough to enable the generation of acceptable reconstructions, but needs to be simple enough to allow for efficient computation. This section analyzes the advantages and disadvantages of several potential system models.

5.2.1 Ideal Model

The ideal system model, which is introduced in section 2.3.1, dictates that an entry a_{ij} in the system matrix is the volume of the intersection between the jth voxel and the path of the ith projection ray. It would be best to compare the resultant system matrices of various system models against the ideal system matrix, but the ideal model was not implemented, so a direct comparison is impossible. Instead, the comparision will be made against a known property of the ideal system matrix.

Consider an ideal system matrix, A, of dimension MxN, and a vector of ones, y, with length M. Then the backprojection operation $x = A^T y$ yields x such that

$$x_j = \sum_{i=1}^{N} a_{ij}\, y_i = \sum_{i=1}^{N} a_{ij}. \tag{5.1}$$

Note that x_j is the jth column sum of A, so x_j denotes the sum of the intersections between the jth voxel and each of the i projection rays. We will refer to this value as the voxel support as it indicates a relative weight for the amount of data support for a given

voxel. For a voxel that lies within the spherical support region (SSR), this value will simply be the volume of a single voxel times the number of projections. Furthermore, voxels that lie partially or fully outside the SSR are set to zero. Thus, for a chosen transaxial slice, all of the x_j's inside the SSR have a non-zero constant value, and all of the x_j's outside of the SSR have the value zero. Therefore, graphing the voxel support for each voxel of a given transaxial slice will yield the support values shown in figure 5.1. In this figure, the SSR is assumed to be 200 voxels wide in the central y plane and the support values are normalized to one. The central y profile is shown in figure 5.2. Note that the ideal voxel support graph for a transaxial slice resembles a top hat. For this reason, we will refer to this property as the top hat property.

We will show in the following section that failure to satisfy the top hat property in a given system model is correlated to artifacts in the reconstruction. Consequently, we can use similarity to this property as a rough metric to test the effectiveness of various system models.

5.2.2 Single Line Intersection Model

We introduced the single line intersection model in section 2.3.2. As noted in that section, this model allows for very fast computation, but produces undesirable ring artifacts. These ring artifacts can be correlated to a failure to satisfy the top hat property of the ideal system matrix.

To test the single line intersection system model, we first compute a matrix A according to the model. We then backproject A over a vector of ones, yielding the column

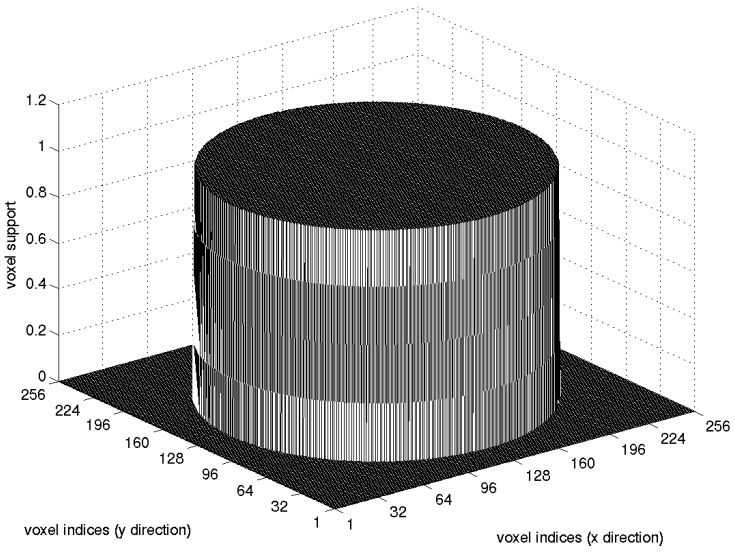

Figure 5.1. Ideal voxel support for a given transaxial slice.

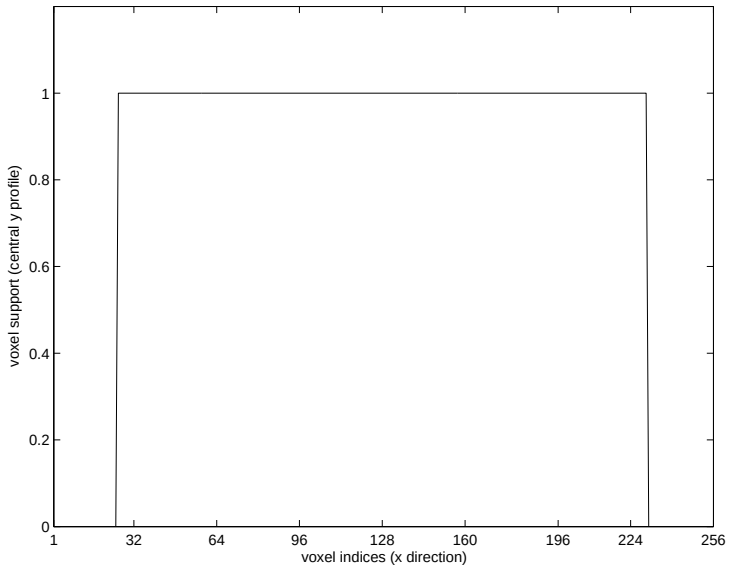

Figure 5.2. Central profile of ideal voxel support.

sums of the matrix. Finally, we plot the voxel support values of a transaxial slice in the backprojected volume.

As a concrete example, we compute the system matrix for a scanner with 256×256 detector cells and a 256^3 reconstruction volume. After backprojecting the resultant system matrix over a vector of ones, we isolate the 99th transaxial slice of the image. The contour lines corresponding to this transaxial slice are plotted in figure 5.3. Also, figure 5.4 corresponds to a profile of figure 5.3 through the central coronal plane.

If the single line intersection technique accurately modeled the top hat property of the ideal system matrix, the contour plot would consist of a single circle corresponding to the periphery of the SSR in this transaxial slice. However, it is evident in figures 5.3 and 5.4 that the single line intersection model does not accurately model the top hat property. There are rings in the contour corresponding to peaks and valleys in the profile and there are also additional radial noise patterns. Lines are drawn tangential to the rings at the central coronal plane. Note that the lines are labelled with the voxel index in the x direction for reference. Drawing equivalent lines in the profile depicts the correlation between the rings of the contour and the peaks and valleys of the profile.

Furthermore, the peaks and valleys in the voxel support values correspond directly to ring artifacts in the reconstructed images. To show this phenomenon, we reconstructed 64 iterations of transaxial slice 99 of the Shepp-Logan phantom using SART and a single line based model. We then clamped the attenuation values to the range $[0.95, 1.05]$ to highlight the structures of the phantom. This reconstruction is shown in figure 5.5 with

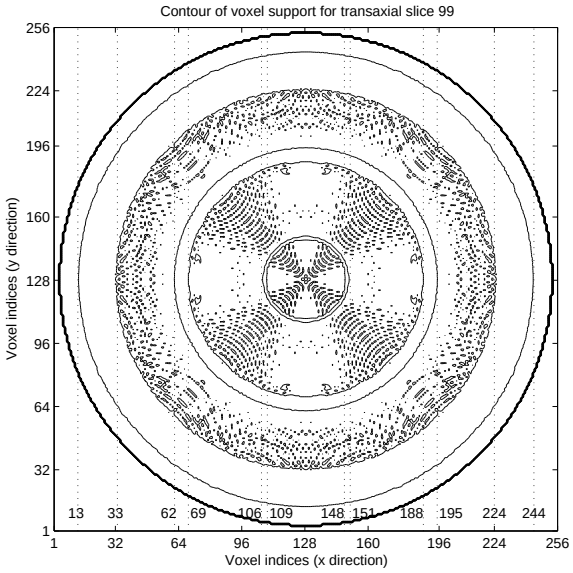

Figure 5.3. Contour of slice 99.

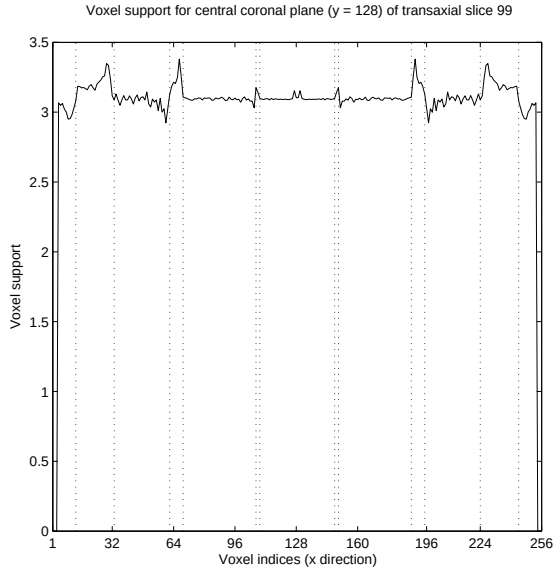

Figure 5.4. Profile of slice 99.

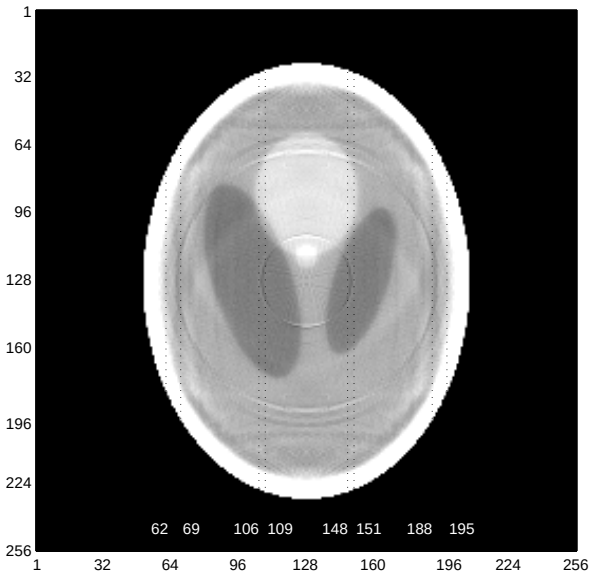

Figure 5.5. Artifacts resulting from single line based model.

vertical dashed lines corresponding to the lines drawn through the contour and profile in figures 5.3 and 5.4. It is evident that the vertical lines correspond to the ring artifacts in the reconstruction. Additionally, the radial noise patterns in the contour plot can also be seen in the reconstruction. Thus, the single line based model is not accurate enough to perform high quality three-dimensional reconstructions.

5.2.3 Multiple Line Intersection Model

As noted in section 2.3.3, computing the intersections for multiple lines per detector cell and averaging the results should approximate the ideal property more closely than the intersection values of a single line. We ran several experiments to test the veracity of this claim as well as to determine how well multiple lines can approximate the property

of the ideal model.

In order to test this, we computed the voxel support values as was done for the single line model using varying numbers of lines. As noted for the ideal case, any voxel in the SSR should have a constant value. Since any voxel not within the SSR can be ignored, the standard deviation of the contained voxels should be zero. Thus, to test similarity between a given number of multiple lines and the ideal case, we calculated standard deviations for the values of the voxels within the SSR. These values are plotted in figure 5.6. As can be seen in this picture, the standard deviations do decrease with an increasing number of lines. Note that the computational burden increases with the number of lines, so there is a tradeoff between a more accurate model and computational cost. Furthermore, note that the standard deviations do not appear to approach zero. We address this issue shortly.

For means of visual comparison, the central profiles of several models are presented in figure 5.7. It is clear in these images that as the number of lines per detector cell increases, the amplitude of the peaks and valleys decreases.

However, an additional problem of the line based models is evident in these profiles. As can be clearly seen in the plots using more lines, there is a slight dip in the voxel support near the center of the profile. This is most likely due to the varying degrees of sampling coverage caused by using line models for divergent geometries. Since the lines diverge away from the X-ray source, coverage in voxels further from the X-ray source will be lower, in relative terms, than coverage in voxels near the X-ray source. This

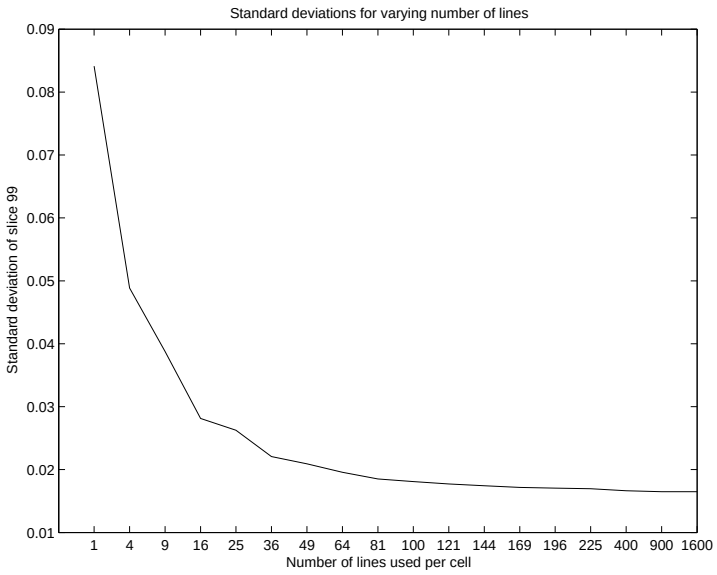

Figure 5.6. Standard deviations for slice 99.

dishing phenomenon also likely explains the apparent failure of the standard deviations to approach zero in the multiple line based models. However, it is not further considered for the purposes of this thesis.

5.2.4 Trilinear Interpolation Model

As introduced in section 2.3.4, the trilinear interpolation model takes a different approach to calculating the system matrix. As a result, the relative voxel support values are not in the same range as the single and multiple line intersection models. In order to facilitate comparing the standard deviation of the trilinear approach to the line intersection approaches, the voxel support values of transaxial slice 99 were modified as

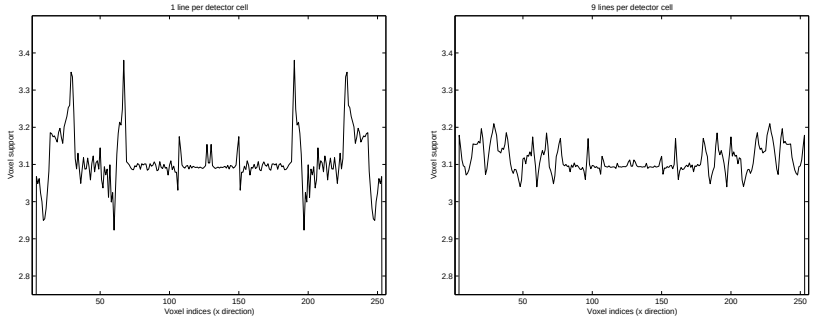

(a) 1 line per cell

(b) 9 lines per cell

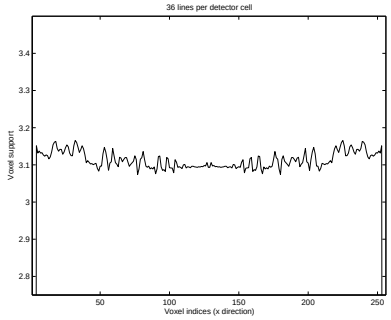

(c) 36 lines per cell

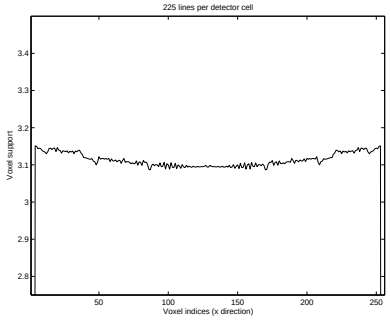

(d) 225 lines per cell

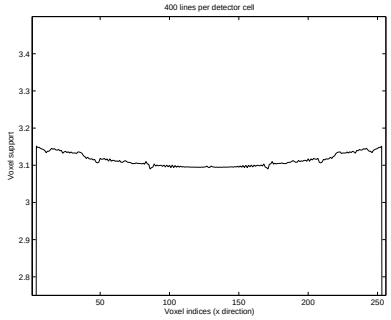

(e) 400 lines per cell

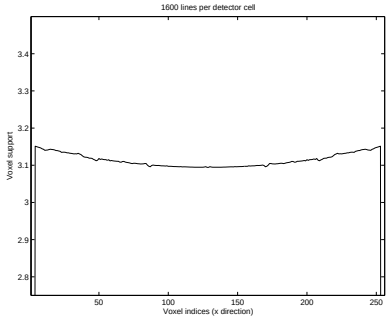

(f) 1600 lines per cell

Figure 5.7. Profiles of voxel support for transaxial slice 99.

follows

$$x_j = x_j * \frac{\mu_{1600}}{\mu_{tri}} \tag{5.2}$$

where x_j is the jth voxel, μ_{1600} is the mean of the voxel support values for the 1600 line intersection model, and μ_{tri} is the mean of the voxel support values for the trilinear approach. After normalizing, the standard deviation for transaxial slice 99 of the trilinear based model was 0.0179. This falls between the standard deviation for the 100 line model, which was 0.0181, and the standard deviation for the 121 line model, which was 0.0177. Due to the spurious assumption in equation (5.2), namely that the system model using 1600 lines is the ideal system model, the standard deviation for the trilinear model cannot be directly compared against the intersection based models. However, this does show that the standard deviation for the trilinear system model is in the same neighborhood as using many lines in the intersection based models.

The voxel support values for the central coronal plane of transaxial slice 99 for the trilinear interpolation model are illustrated in figure 5.8. Note that this profile includes central dishing similar to the multiline profiles.

5.3 3D Shepp-Logan Phantom Reconstructions

The 3D Shepp-Logan phantom is a well-known analytical phantom consisting of 10 ellipsoids of varying sizes, orientations, and attenuation coefficients used to verify re-

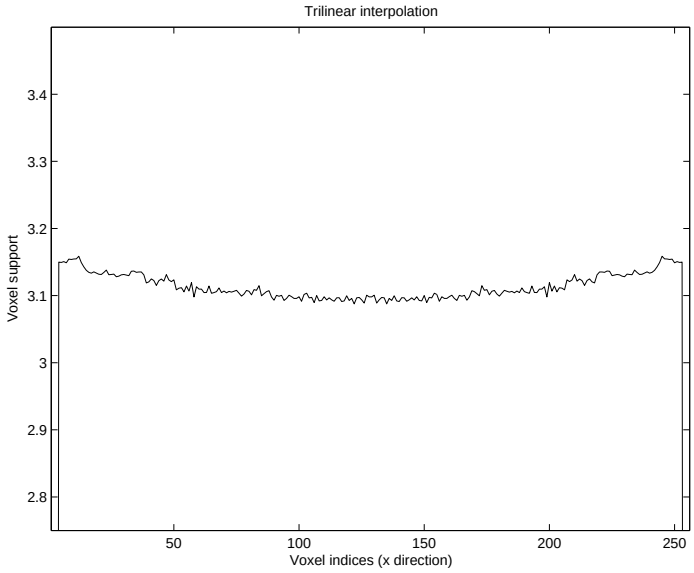

Figure 5.8. Trilinear interpolation voxel support.

construction models and algorithms. Although computing a 3D reconstruction for a full half of the phantom, we will focus on transaxial slice 99, which is shown in figure 5.9. The 64th iteration of SART, EM, and FWLS using trilinear interpolation and a multiline model with 144 lines per detector cell are illustrated in figure 5.10. We clamped the attenuation coefficients of each of these images to the range $[0.95, 1.05]$ before displaying to highlight the internal structures. Furthermore, we normalized the trilinear interpolation based models by the mean of the ideal phantom, similarly to equation (5.2).

There are several features worthy of note in these reconstructions. First of all, none of the reconstruction algorithm and system model combinations faithfully reconstructed the lower two ellipsoids, although the remaining ellipsoids were accurately

Figure 5.9. Original phantom.

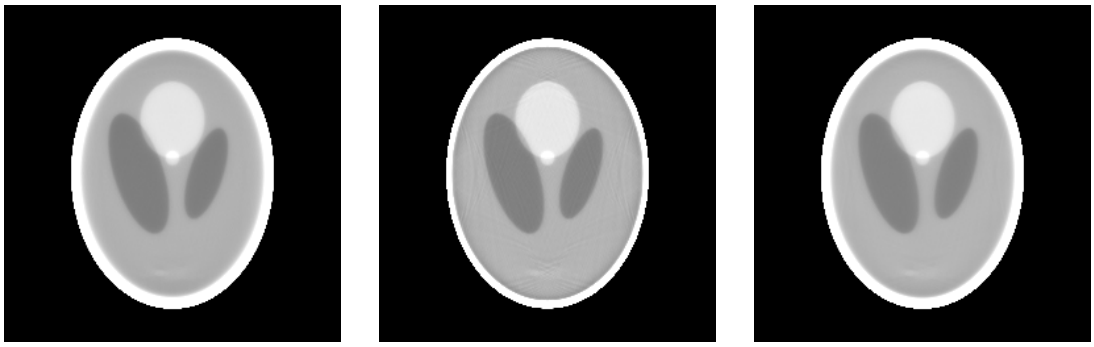

(a) Trilinear/SART (b) Trilinear/EM (c) Trilinear/FWLS

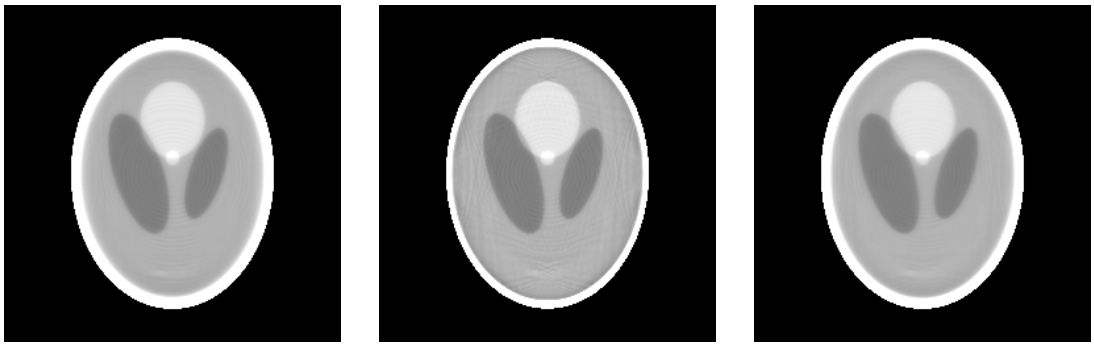

(d) Multiline/SART (e) Multiline/EM (f) Multiline/FWLS

Figure 5.10. Phantom reconstructions of transaxial slice 99.

reconstructed. There is, however, a noticable change in the attenuation coefficients in the area of the ellipsoids, which would hopefully draw attention to the area. Secondly, the EM reconstructions, using both system models, were slightly noisier than the other reconstructions. This may be due to using the emission derived EM algorithm rather than a transmission derived algorithm. Thirdly, there is visible ringing in the reconstructions using multiple lines, although it is not as severe as for the single line model. Using more lines should gradually improve the reconstructions. Lastly, the outermost ellipsoid is wider in the reconstructions than in the original. This is more pronounced when using SART and FWLS. To explain this, we analyze profiles of the reconstructed images.

In figure 5.11, we plot profiles of coronal slice 114 of the attenuation coefficients of the reconstructed images against the known values. In the SART and FWLS reconstructions, the reconstructed values are not tight to the abrupt change in attenuation values at the edge of the outermost ellipsoid. Thus, when we clamp the attenuation values to the range $[0.95, 1.05]$, the outermost ellipsoid appears wider than it should. However, this is more of an artifact associated with the clamping than the reconstruction.

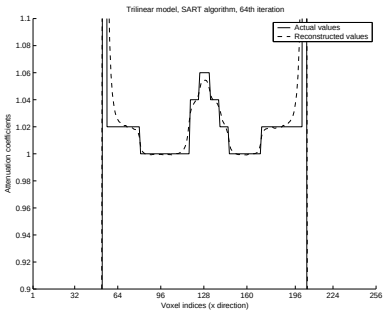

(a) Trilinear/SART

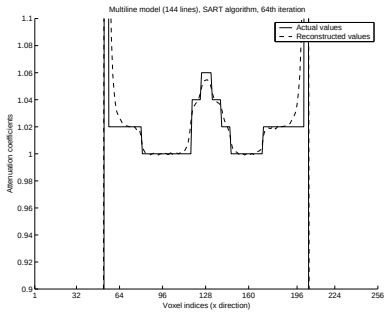

(b) Multiline/SART

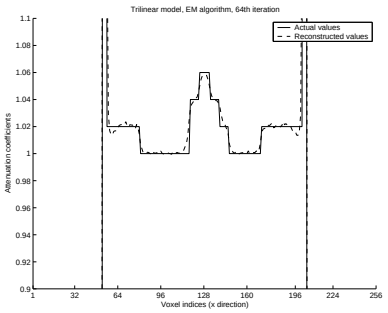

(c) Trilinear/EM

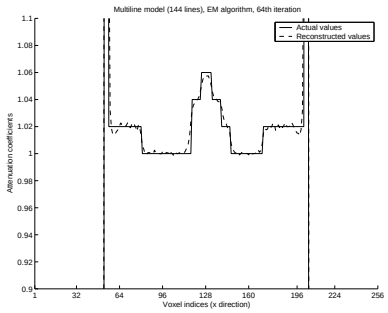

(d) Multiline/EM

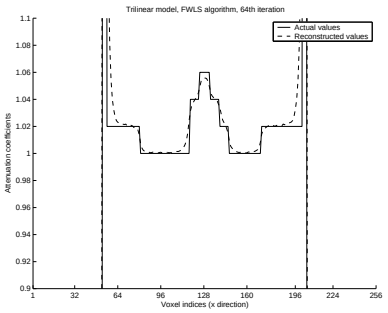

(e) Trilinear/FWLS

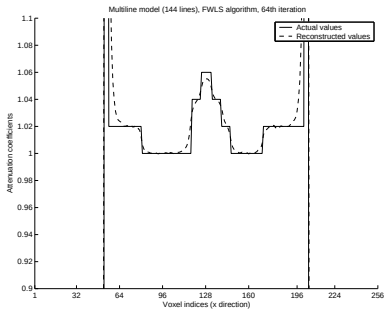

(f) Multiline/FWLS

Figure 5.11. Profiles of transaxial slice 99, coronal slice 114.

5.4 Mouse Data Reconstructions

While the Shepp-Logan phantom is useful as a means of testing reconstruction algorithms and system models, it does not realistically model the process of attenuation occurring during the aquisition of real data. The phantom projection data is noiseless and based upon line integrals, which is not physically accurate. Thus, we also tested the framework using X-ray CT data collected from a mouse scan using the MicroCAT scanner.

The projection data has dimensions 512×1022. We reconstructed half of the volume at 256×256 resolution per transaxial slice, so the voxel space has dimensions $256 \times 256 \times 512$. We ran each algorithm to 64 iterations using the same algorithms and system models as in the previous section. Some results are shown in figures 5.12 and 5.13 for transaxial slices 350 and 450, respectively. Since the system matrix grew too large to store in main memory during the mouse reconstructions, the system matrix was stored on disk and read incrementally.

The attenuation coefficients of the EM produced images were clamped to the same range as the SART produced images to facilitate visual comparison. Otherwise, the EM images would be slightly darker than the SART and FWLS images after conversion to gray level values. Unfortunately, there is no known set of correct images to compare against these reconstructions. However, the reconstructions demonstate that the framework is capable of handling real world CT data.

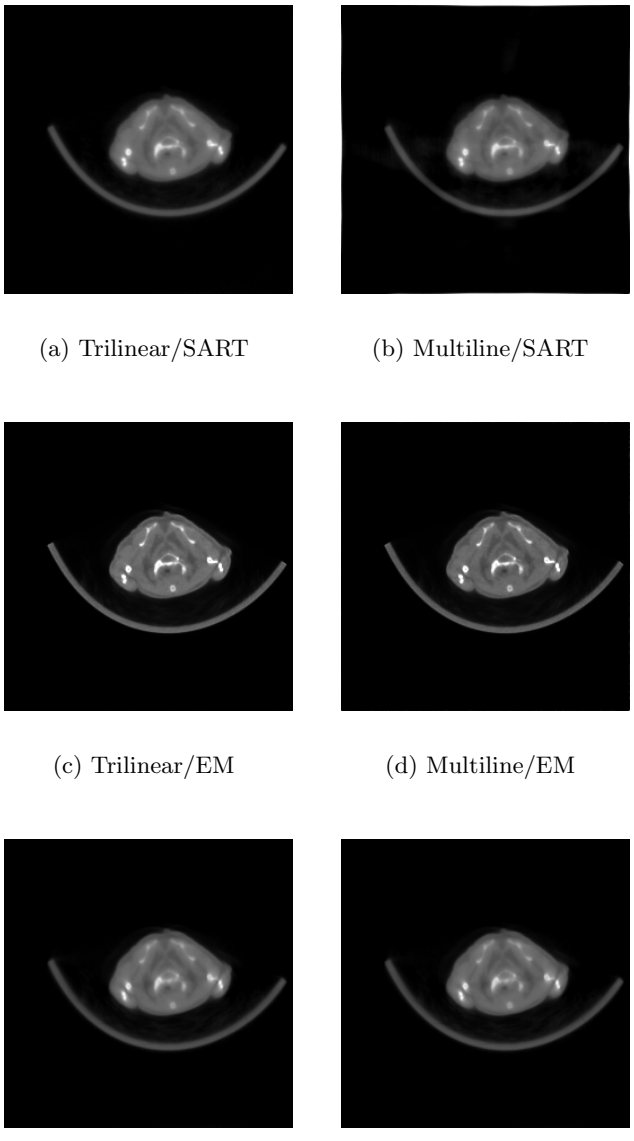

(a) Trilinear/SART (b) Multiline/SART

(c) Trilinear/EM (d) Multiline/EM

(e) Trilinear/FWLS (f) Multiline/FWLS

Figure 5.12. Mouse reconstuctions (transaxial slice 350).

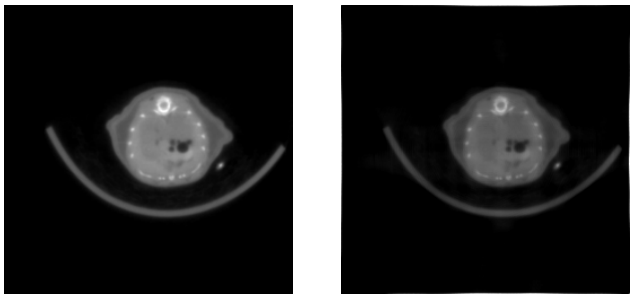

(a) Trilinear/SART (b) Multiline/SART

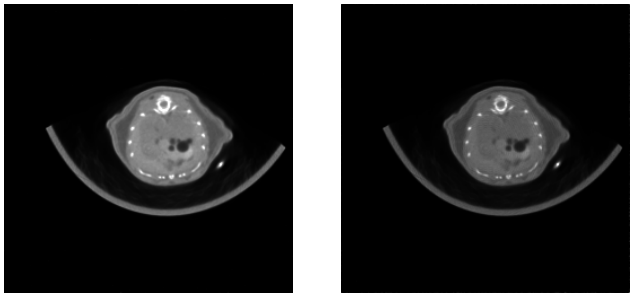

(c) Trilinear/EM (d) Multiline/EM

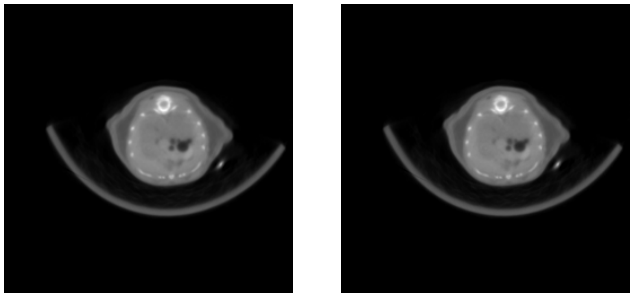

(e) Trilinear/FWLS (f) Multiline/FWLS

Figure 5.13. Mouse reconstuctions (transaxial slice 450).

Table 5.1

System matrix storage requirements.

	Trilinear Interpolation	Multiline Intersection
Phantom Data		
Number of elements stored	$1,011,298,717$	$812,056,052$
Approximate storage (bytes)	$\approx$ 8GB	$\approx$ 6.5GB
Mouse Data		
Number of elements stored	$13,430,851,808$	$8,662,072,989$
Approximate storage (bytes)	$\approx$ 107.5GB	$\approx$ 70GB

5.5 Storage Analysis

As noted previously, each of the 23 nodes used for the reconstruction has 2GB of RAM. Thus, the size of the system matrix is bound above by 46GB for storage in main memory. Note that in reality the limit is lower than this due to the overhead of other storage.

For the Shepp-Logan phantom reconstructions, the matrix is small enough to store in main memory. However, for the mouse data reconstructions, the matrix must be stored on disk. The total number of elements and approximate memory requirements for the phantom and mouse reconstructions are given in table 5.1. The multiple line model used 144 lines per detector cell. Note that the values in the table correspond to the number of elements stored, not the total number of elements in the system matrix. Due to symmetries, the total number of system matrix elements is approximately eight times that of the number of elements stored.

One additional interesting statistic involving the number of system matrix elements is the distribution of these elements among the cluster nodes. This is plotted in figure 5.14 for the trilinear interpolation system model used for the mouse reconstruction.

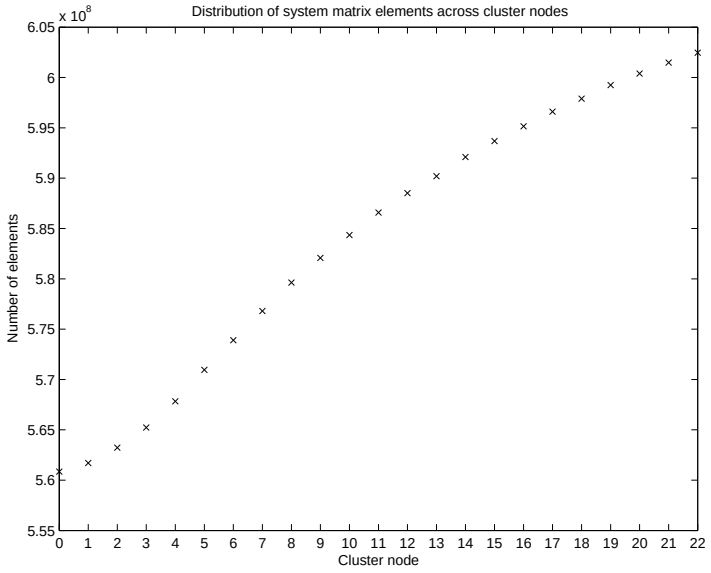

Figure 5.14. Distribution of system matrix across cluster nodes.

Ideally, this distribution would be almost uniform. However, in this case, the higher numbered nodes have more matrix elements than the lowered numbered nodes. This is a result of distributing the data based on projections. As the view angle increases toward 45°, the number of intersections of the projection rays with the voxel space increases due to the increase in the total intersection length of the projection rays with the voxel space. In this example, the node with the most data manages approximately 7% more data than the node with the least amount of data. Modest performance gains may be achieved by distributing the data more uniformly, but that is not explored in this thesis.

5.6 Performance Analysis

We performed an analysis of the performance of system model construction and the iterations of the EM algorithm. We further subdivide the iterative phase by the projector operations and MPI communication. The EM algorithm includes one forward and backprojector per iteration, plus an extra initial backprojection for scaling purposes. This is typical of the iterative algorithms and can thus be used to gauge the performance of the iterative framework.

5.6.1 System Model Analysis

In order to evaluate the performance of the system model construction, we ran several experiments using the same scanner configuration as for the Shepp-Logan phantom above. Recall that this includes a 256×256 detector and that each MPI node is responsible for calculating system model data for two projections. Thus, each node must calculate line intersection data for $131,072$ projection rays in the single line and trilinear interpolation models. For multiple line models, this number scales with the number of lines per detector cell.

Recall that with the multiple line intersection based models, the values stored in the system matrix are the averages of the intersection lengths of each of the lines with a given voxel. Thus, in addition to the line intersection computation code, there must be row averaging code to compute the final row to be stored in the system matrix. The total system matrix computation time is the sum of the intersection computation

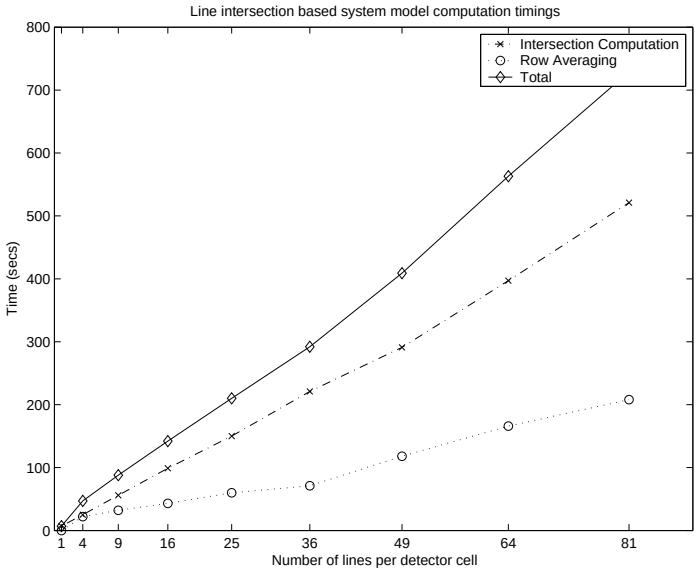

Figure 5.15. Line intersection based system model computation timings.

time and the row averaging time. These times are plotted in figure 5.15 for increasing numbers of lines per detector cell. The times plotted were recorded from node 22. As shown in figure 5.14, this node computes the most data and will subsequently have the longest run times.

Note that the line intersection computation scales almost perfectly linearly, with the row averaging curve slightly below. The result is that the system matrix computation time for the line intersection based models scales very well.

The trilinear interpolation model took 90 seconds to compute with the same geometry as above. This places the trilinear interpolation model between the 9 and 16 multiple line models in terms of computational cost.

The system model calculation currently only uses a single processor per node. Since

the cluster nodes each have two processors, performance gains could be achieved by distributing the system matrix calculation between the two processors.

5.6.2 Iteration Analysis

Each iteration of the typical iterative reconstruction algorithms includes a single forward and backprojection as well as one MPI communication following the backprojection. The EM algorithm matches this behavior and was thus chosen as a representative algorithm for performance analysis. Note that the EM algorithm also includes a single backprojection before the first iteration for scaling purposes.

Since the size of the system matrix for the Shepp-Logan phantom reconstructions is relatively small, we store the matrix in main memory. Thus, the computation in the projectors consists of recovering the matrix from the symmetries and performing the necessary multiplications. The other major cost per iteration is the MPI communication. To measure the performance of these operations, we ran the EM algorithm on the Shepp-Logan phantom data using the trilinear interpolation model for 32 iterations. To get approximate relative costs, we averaged the timings for each projector and the MPI communication across all nodes. The resulting approximate cost per iteration is shown in figure 5.16.

As the system matrix size increases, it must be stored to disk rather than in main memory. The need to read the system matrix from disk on demand will significantly increase the time spent in the projectors. Since the system matrix for the mouse reconstructions was large enough to require disk storage, we use it to gauge the performance

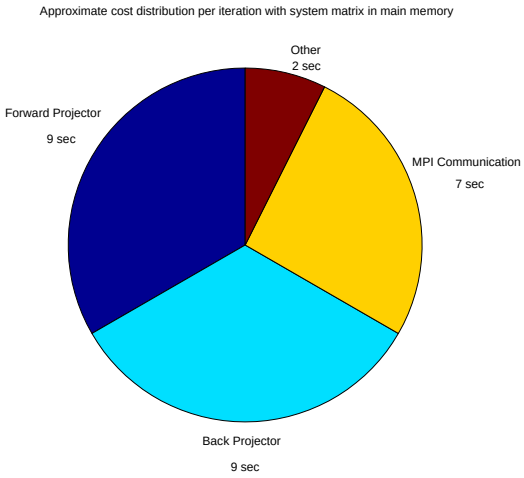

Figure 5.16. Cost distribution per iteration (main memory).

impact of disk storage. For this experiment, we ran the EM algorithm on the mouse data using the trilinear interpolation model for 4 iterations. We again averaged the costs per iteration. The results are shown in figure 5.17. Recall from table 5.1 that the system matrix for the mouse reconstruction was approximately 13 times larger than for the Shepp-Logan phantom. Thus, if the system matrix were stored in main memory, we would expect the cost per iteration of each projector to increase by a factor of about 13. It in fact increases by a factor of almost 24, so the disk access nearly doubles the cost of the projectors in this case.

5.6.3 Overall Performance

The total run time for 32 iterations of the Shepp-Logan phantom data using the trilinear interpolation model was approximately 16.5 minutes. With an average iteration time

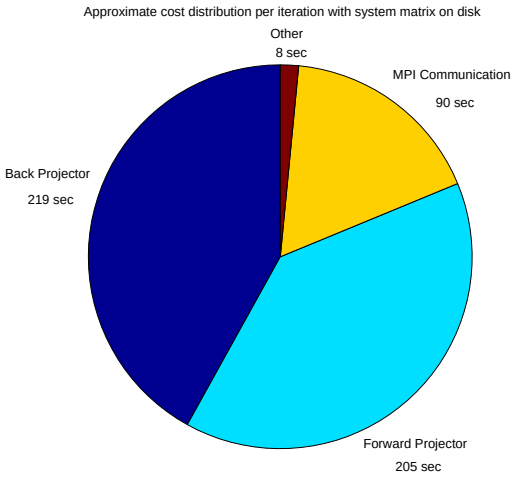

Figure 5.17. Cost distribution per iteration (disk storage).

of 27 seconds and a system model computation time of 90 seconds, this leaves just over half a minute for overhead related to reading the projection data, calculating the scaling factors, and other setup procedures. Note that if this same system model was used, but the system matrix was recomputed rather than stored, the average iteration time would be at least 180 seconds since the matrix is needed twice per iteration.

The total run time for 4 iterations of the mouse data using the trilinear interpolation model was approximately 42.5 minutes. The average iteration time was just over 8.5 minutes. Thus, the overhead in this case was nearly 8.5 minutes. The increase in overhead is due to the larger projection data set and the costly scaling factor computation, which is accomplished with a backprojection. In addition to the 42.5 minute reconstruction, the system model generation took about 13.5 minutes, although this cost can be absorbed before performing the reconstruction. Computing the same system matrix on

the fly would therefore slow the iterations to at least 27 minutes. Thus, even with the cost associated with disk storage, the per iteration cost is much lower in this case than if we recomputed the matrix on demand. If a simple enough system model is chosen, the on the fly computation may perform better than disk storage, but the model would likely yield inferior reconstruction results.

Chapter 6

Conclusions and Future Work

In this work, we accomplished the overall goal of building a framework to support high-resolution iterative CT data reconstructions. The reconstructions of the mouse CT data exhibit that the framework is capable of managing problems of significant size. However, the storage and computational requirements are likely still too high for clinical deployment. As computer technology progresses, the requirements will become easier to satisfy.

Of the system models analyzed, trilinear interpolation seems to be the most promising. While the storage requirements are higher than for the line intersection based models, the computational advantage over using an adequate number of lines is significant. We could also lower the computational and storage requirements by decreasing the Δ_s value used for the interpolation, although that would require re-analyzing the system model with respect to accuracy. Furthermore, we observed no undesirable ef-

fects in regards to the trilinear interpolation model during this work. However, a more rigorous analysis of the smoothing effects of this model are in order.

Since analyzing various algorithms was not a goal of this thesis, little work was performed in this regard. However, now that the framework has been developed, there are many possibilities for future work, including comparative analysis of various algorithms.

One possible area of future work involves improving the current system models as well as developing and analyzing new system models. As noted in chapter 2, each of the current system models includes central dishing in the voxel support values. Compensating for this dishing may increase the quality of the generated system matrices. Furthermore, researching possible methods for calculating the ideal system matrix based on volumetric intersections is another possibility for future research. Even if the computational cost is high, an ideal system model would be useful for comparative purposes.

In addition to continued system model research, the set of available algorithms can be expanded and more rigorous analyses performed. For example, penalties can be included in most iterative algorithms for regularization purposes. Moreover, additional algorithms can be added to the framework. For example, work has been performed by Nuyts et al. to derive solutions to the transmission EM algorithm using regular forward and backprojectors [9]. It would be interesting to compare this algorithm to the EM algorithm implemented in this thesis. Furthermore, we could perform a more rigorous comparison of algorithms using a real data phantom as opposed to the analytical Shepp-Logan phantom. A comparative analysis of the iterative algorithms to FBP is

also warranted.

Finally, there are several areas of further research with regards to the current implementation. As noted in section 5.5, the current load distribution is not ideal. Further equalizing the distribution would increase performance. Also, the inclusion of checkpointing support would be beneficial. Currently, if the program terminates unexpectedly, it cannot restart at the point of failure. The generated data is available, but all of the work must be repeated to perform additional iterations. It should be possible to save the voxel space data and use it to bootstrap the iterative algorithms.

The development of the iterative framework enables further research into any of these areas.

Bibliography

Bibliography

[1] R. Barrett, M. Berry, T. F. Chan, J. Demmel, J. Donato, J. J. Dongarra, V. Eijkhout, R. Pozo, C. Romine, and H. van der Vorst. *Templates: Building Blocks for Iterative Methods*. SIAM, Philadelphia, PA, 1993.

[2] I. A. Elbakri and J. A. Fessler. Statistical image reconstruction for polyenergetic x-ray computed tomography. *IEEE Trans. on Med. Imag.*, 21(2):89–99, February 2002.

[3] L. A. Feldkamp, L. C. Davis, and J. W. Kress. Practical cone-beam algorithm. *J. Opt. Soc. Amer.*, 1:612–619, 1984.

[4] S.S. Gleason, H. Sari-Sarraf, M. J. Paulus, D.K. Johnson, S.J. Norton, and M. A. Abidi. Reconstruction of multi-energy x-ray computed tomography images of laboratory mice. *IEEE Transactions on Nuclear Science*, 46(4):1081–1086, August 1999.

[5] F. Jacobs, E. Sundermann, B. De Sutter, M. Christiaens, and I. Lemahieu. A fast algorithm to calculate the exact radiological path through a pixel or voxel space.

[6] A. C. Kak and M. Slaney. *Principles of Computerized Tomographic Imaging*. Society of Industrial and Applied Mathematics, 2001.

[7] K. Lange and R. Carson. Em reconstruction algorithms for emission and transmission tomography. *Journal of Computer Assisted Tomography*, 8(2):306–316, April 1984.

[8] L. B. Lucy. An iterative technique for the rectification of observed distributions. *The astronomical journal*, 79(6):745–754, June 1974.

[9] J. Nuyts, B. De Man, P. Dupont, M. Defrise, P. Suetens, and L. Mortelmans. Iterative reconstruction for helical ct: a simulation study. *Phys. Med. Biol.*, 43(4):729–737, 1998.

[10] M. J. Paulus, H. Sari-Sarraf, S. S. Gleason, M. Bobrek, J. S. Hicks, D. K. Johnson, J. K. Behel, L. H. Thompson, and W. C. Allen. A new x-ray computed tomography system for laboratory mouse imaging. *IEEE Transactions on Nuclear Science*, 46(3):558–564, June 1999.

[11] W. H. Richardson. Bayesian-based iterative method of image restoration. *Journal of the Optical Society of America*, 62(1):55–59, January 1972.

[12] L. A. Shepp and Y. Vardi. Maximum likelihood reconstruction for emission tomography. *IEEE Trans. on Med. Imag.*, MI-1(2):113–122, October 1982.

[13] R. L. Siddon. Fast calculation of the exact radiological path for a three-dimensional ct array. *Medical Physics*, 12(2):252–255, 1985.

[14] G. Wang, C. R. Crawford, and W. A. Kalender. Multirow detector and cone-beam spiral/helical ct. *IEEE Trans. on Med. Imag.*, 19(9):817–821, Sept. 2000.

[15] G. Wang, D. L. Snyder, J. A. O'Sullivan, and M. W. Vannier. Iterative deblurring for ct metal artifact reduction. *IEEE Trans. on Med. Imag.*, 15(5):657–663, October 1996.

[16] G. L. Zeng and G. T. Gullberg. A study of reconstruction artifacts in cone beam tomography using filtered backprojection and iterative em algorithms. *IEEE Trans. on Nucl. Sci.*, 37(2):759–767, 1990.

[17] G. L. Zeng and G. T. Gullberg. Unmatched projector/backprojector pairs in an iterative reconstruction algorithm. *IEEE Trans. on Med. Imag.*, 19(5):548–555, 2000.

Vita

Thomas Matthew Benson was born in Greeneville, TN. He attended grade school and high school there and received a high school diploma from Greeneville High School in 1997. He subsequently attended the University of Tennessee, Knoxville, where he completed Bachelor of Science degrees with highest honors in Computer Science and Mathematics in May 2001. He is continuing his work at the university toward a doctorate in Computer Science.